#### **OPEN ACCESS**



# Accretion Flows or Outflow Cavities? Uncovering the Gas Dynamics around Lupus 3-MMS

Travis J. Thieme<sup>1,2,3</sup>, Shih-Ping Lai<sup>1,2,3,4</sup>, Sheng-Jun Lin<sup>1,2,3</sup>, Pou-Ieng Cheong<sup>1,3</sup>, Chin-Fei Lee<sup>4,5</sup>, Hsi-Wei Yen<sup>4</sup>, Zhi-Yun Li<sup>6</sup>, Ka Ho Lam<sup>6</sup>, and Bo Zhao<sup>7</sup>

<sup>1</sup> Institute of Astronomy, National Tsing Hua University, No. 101, Section 2, Kuang-Fu Road, Hsinchu 30013, Taiwan
<sup>2</sup> Center for Informatics and Computation in Astronomy, National Tsing Hua University, No. 101, Section 2, Kuang-Fu Road, Hsinchu 30013, Taiwan
<sup>3</sup> Department of Physics, National Tsing Hua University, No. 101, Section 2, Kuang-Fu Road, Hsinchu 30013, Taiwan
<sup>4</sup> Academia Sinica Institute of Astronomy and Astrophysics, P.O. Box 23-141, Taipei 10617, Taiwan
<sup>5</sup> Graduate Institute of Astronomy and Astrophysics, National Taiwan University, No. 1, Section 4, Roosevelt Road, Taipei 10617, Taiwan
<sup>6</sup> Department of Astronomy, University of Virginia, 530 McCormick Road, Charlottesville, Virginia 22904-4325, USA
<sup>7</sup> Department of Physics and Astronomy, McMaster University, 1280 Main Street, West Hamilton, Ontario L8S 4L8, Canada
Received 2021 June 26; revised 2021 October 27; accepted 2021 November 5; published 2022 January 21

#### Abstract

Understanding how material accretes onto the rotationally supported disk from the surrounding envelope of gas and dust in the youngest protostellar systems is important for describing how disks are formed. Magnetohydrodynamic simulations of magnetized, turbulent disk formation usually show spiral-like streams of material (accretion flows) connecting the envelope to the disk. However, accretion flows in these early stages of protostellar formation still remain poorly characterized, due to their low intensity, and possibly some extended structures are disregarded as being part of the outflow cavity. We use ALMA archival data of a young Class 0 protostar, Lupus 3-MMS, to uncover four extended accretion flow–like structures in C<sup>18</sup>O that follow the edges of the outflows. We make various types of position–velocity cuts to compare with the outflows and find the extended structures are not consistent with the outflow emission, but rather more consistent with a simple infall model. We then use a dendrogram algorithm to isolate five substructures in position–position–velocity space. Four out of the five substructures fit well (>95%) with our simple infall model, with specific angular momenta between  $2.7-6.9 \times 10^{-4} \, \mathrm{km \, s^{-1}}$  pc and mass-infall rates of  $0.5-1.1 \times 10^{-6} \, M_{\odot} \, \mathrm{yr}^{-1}$ . Better characterization of the physical structure in the supposed "outflow cavities" is important to disentangle the true outflow cavities and accretion flows.

*Unified Astronomy Thesaurus concepts:* Accretion (14); Circumstellar disks (235); Observational astronomy (1145); Radio astronomy (1338); Radio interferometry (1346); Protostars (1302); Star formation (1569); Stellar accretion (1578); Stellar accretion disks (1579); Young stellar objects (1834)

Supporting material: animations

#### 1. Introduction

Rotationally supported disks around the youngest protostars are essential for transporting the angular momentum of infalling material from the envelope to the protostar and for the development of protoplanetary systems. Observations of molecular lines trace the Keplerian rotation of these disks around Class 0 protostars and confirm that disks form in the earliest stages of star formation when the protostar is still deeply embedded in its parent core (e.g., Tobin et al. 2012b; Murillo et al. 2013; Codella et al. 2014; Lee et al. 2014; Ohashi et al. 2014; Aso et al. 2017; Yen et al. 2017a). The sizes of these gaseous disks in the Class 0 stage range from about 20 to 150 au around protostellar masses less than  $0.5 M_{\odot}$ . As the protostar evolves into the later Class I phase, the observed disk radii range between 50 to 700 au around protostellar masses less than  $2.5 M_{\odot}$  (e.g., Lommen et al. 2008; Harsono et al. 2014; Yen et al. 2015). The wide range of disk radii shows that their formation is complicated and can have a variety of outcomes. In order to better understand the formation and

Original content from this work may be used under the terms of the Creative Commons Attribution 4.0 licence. Any further distribution of this work must maintain attribution to the author(s) and the title of the work, journal citation and DOI.

growth of these young disks, it is important to study how material accretes onto the disk from the surrounding envelope.

A rotationally supported disk (hereafter, RSD) is expected to form around the protostar, due to the conservation of angular momentum (e.g., Ulrich 1976). In this simplified model of axisymmetric gravitational collapse, the infalling materials follow freefall parabolic trajectories that collide with the disk under the assumption that the central object can be approximated as a point source (CMU Model; see Ulrich 1976; Cassen & Moosman 1981). Under the "inside-out" assumption (Shu 1977), the disk radius is then expected to grow as  $\propto M_{\rm sd}^3$ , where  $M_{\rm sd}$  is the total mass of the star+disk system (Terebey et al. 1984). While this CMU model can describe the kinematics of the infalling material, it is possible for the material to fall in from every direction around the disk in a globalized collapse scenario, or in filamentary-like streams due to asymmetric density structures in the envelope (Tobin et al. 2012a). On the other hand, magnetohydrodynamic (MHD) simulations of dense cores show spiral-like streams of material connecting the envelope to the disk in magnetized turbulent cores (Li et al. 2014; Seifried et al. 2015). These models show that the accretion flow structures, as well as the formation of a rotationally supported disk, can vary depending on the levels of turbulence and magnetic fields in the system. In the ideal MHD limit, if the magnetic field is strongly coupled with the rotating

gas within the protostellar core, it becomes twisted and can effectively carry away angular momentum from the central region and inhibit the formation of protostellar disks (Magnetic Braking Catastrophe; see Mellon & Li 2008; Hennebelle & Fromang 2008). Several mechanisms have been proposed to weaken the magnetic braking effect and allow for the formation of protostellar disks of comparable sizes to those previously observed, including turbulence (e.g., Joos et al. 2013; Seifried et al. 2013), misalignment between the magnetic field and rotation axis (e.g., Hennebelle & Ciardi 2009; Li et al. 2013), nonideal MHD effects (e.g., Li et al. 2011; Wurster et al. 2016), microphysics (e.g., Zhao et al. 2016; Wurster et al. 2018; Kuffmeier et al. 2020), and various combinations of these scenarios (e.g., Tsukamoto et al. 2018; Lam et al. 2019; Wurster & Lewis 2020). Simulations with these properties to overcome magnetic braking almost always show accretion flows at various stages of their time evolution. Thus, looking for these structures around young protostars and comparing with models can help us to better understand the disk formation

Observationally, these accretion flow-like structures have been reported in a few Class I protostars (L1489-IRS: Yen et al. 2014; HL Tau: Yen et al. 2017b, 2019) and Class 0 protostars (VLA1623: Cheong 2018; Hsieh et al. 2020; IRAS 03292 +3039: Pineda et al. 2020; IRAS 16293-2422: Murillo et al. 2021). In L1489-IRS, Yen et al. (2014) found two infalling flows with lengths of 5000 au (redshifted flow) and 2000 au (blueshifted flow) in  $C^{18}O$  ( $J=2\rightarrow 1$ ). They find these flows are consistent with the CMU model using a centrifugal radius of 300 au. They estimate the mass infalling rate to be  $4-7 \times 10^{-7} M_{\odot} \text{ yr}^{-1}$ . In HL Tau, Yen et al. (2017b, 2019) found two infalling flows in <sup>13</sup>CO ( $J=2 \rightarrow 1$ ), one of which is also seen in HCO  $^+(J=3\rightarrow 2)$ . The  $^{13}$ CO accretion flows can be matched with the CMU model with a centrifugal radius of 100 au and a specific angular momentum of  $1.9 \times$  $10^{-3}$  km s<sup>-1</sup> pc. They estimate the mass infalling rate to be  $2.2 \times 10^{-6} \, M_{\odot} \, \mathrm{yr}^{-1}$ . In VLA1623, Cheong (2018) identify two accretion flows in  $C^{18}O$  ( $J=2\rightarrow 1$ ), using a clump-finding "dendrogram" algorithm (Rosolowsky et al. 2008), that are consistent with the CMU model using a centrifugal radius of 170 AU. The blue and redshifted flows were found to have lengths greater than 1200 au with specific angular momentum of  $2.3-2.9 \times 10^{-3} \,\mathrm{km \, s^{-1}}$  pc and a mass accretion rate onto the disk of  $1.2 \times 10^{-6} M_{\odot} \text{ yr}^{-1}$ . Finally, in IRAS 03292+3039, Pineda et al. (2020) find an asymmetric streamer in  $HC_3N(J=10 \rightarrow 9)$  with a length of  $\sim 10,500$  au that matches the CMU model in the inner part, and seems to have less velocity than expected by the model in the outer part. They estimate the mass-infall rate of the streamer to be  $\sim 10^{-6} M_{\odot} \,\mathrm{yr}^{-1}$ , comparable to the other observed accretion flows. They also consider two different accretion scenarios, where the streamers seen are either part of the parental dense core or coming from beyond the parent dense core. They postulate that, because the molecules detected in the accretion flow are "chemically fresh," the streams are coming from outside the dense core, where they do not have a chance to be depleted. While we have a few examples of these infalling accretion flows, many others report extended structures around other sources, but they are often disregarded as being part of the outflow cavity, due to their proximity to the observed molecular outflows (Yen et al. 2017a; Le Gouellec et al. 2019; Hull et al. 2020). Since everything is projected onto the plane

of the sky, it is not immediately apparent whether these emission are truly connected to the outflow or actually infalling material

In this paper, we seek to explore this issue by using ALMA archival data of CO isotopologues (C<sup>18</sup>O, <sup>13</sup>CO, and <sup>12</sup>CO) along with SO to study the velocity components of extended emission around a young Class 0 source with a confirmed Keplerian disks, Lupus 3-MMS (IRAS 16059-3857) and compare with a simple analytical infall model (CMU Model; see Section 4.1 for a complete description). Lupus 3-MMS is a Class 0 protostar in the Lupus III molecular cloud with  $T_{\rm bol} = 39 \,\mathrm{K}$  and  $L_{\rm bol} = 0.41 \,L_{\odot}$  (Dunham et al. 2013). Yen et al. (2017a) find a Keplerian disk radius of 130 au around a protostellar mass of  $0.3 M_{\odot}$  from kinematic modeling of C<sup>18</sup>O. They also mention seeing extensions in C<sup>18</sup>O with lengths of 2''-4'' along the cavity wall of the outflow, though they do not analyze these structures. The kinematic evidence of a rotationally supported disk, the available archival observations of molecular lines used to identify accretion flows in other sources, and some hints at possible extended structures make this a promising source for our purpose.

The outline of this paper is as follows. Section 2 describes the archival data used along with the calibration and image cleaning process. Section 3 shows the resulting image maps and identifies the different extended structures around our source. Section 4 compares the velocity of the extended structures we found to the outflow velocity structure and also to a simple infall model. Section 5 discusses the analysis of our model, previously observed accretion flows around other sources, and MHD simulations. Section 6 summarizes the paper and our main conclusions.

#### 2. Observations

We use previously observed spectral line data of Lupus 3-MMS from the ALMA archive (Project ID: 2013.1.00879.S, PI: Hsi-Wei Yen). The baseline lengths at 220 GHz range from 18 m to 646 m (13 k $\lambda$  to 498 k $\lambda$ ). These correspond to maximum recoverable scales of  $\sim 6.2$  and  $\sim 5.9$ , respectively. The pointing center was R.A.  $(J2000) = 16^h09^m18^s07$  and decl.  $(J2000) = -39^{h}04^{m}51^{s}6$ . We focus on three of the observed spectral windows centered on different molecular lines that show detections:  $C^{18}O$   $(J=2 \rightarrow 1)$ ,  $^{12}CO$  $(J=2\rightarrow 1)$ , and SO  $(J=5_6\rightarrow 4_5)$ . The calibration was done by using the Common Astronomy Software Applications (CASA; v5.1.2+4.6.2) to run the calibration script provided with the data (McMullin et al. 2007). Self-calibration was not applied. The calibrated molecular line data have channel widths of 61 kHz. We performed continuum subtraction of the molecular line data using the continuum spectral window and the line-free channels of the molecular line spectral windows using the CASA task "uvcontsub." The data were cleaned using the CASA task "tclean" with natural weighting to give slightly lower resolution but have the best signal-to-noise ratio after performing the Fourier transform. We used the default "hogbom" deconvolver and applied a UV taper of  $100 \text{ k}\lambda$ . This taper weights the visibilities to shorter baselines ( $<100 \text{ k}\lambda$ ) and is done in order to try to reveal more extended structure around the source. We tested other UV tapers and found that tapers >100 k $\lambda$  resolved out most of the extended emission and tapers  $<100 \,\mathrm{k}\lambda$  became too noisy due to the sensitivity decreasing from downweighting the data. We produce four molecular line image cubes, each with an image size of 320 pixels, a cellsize

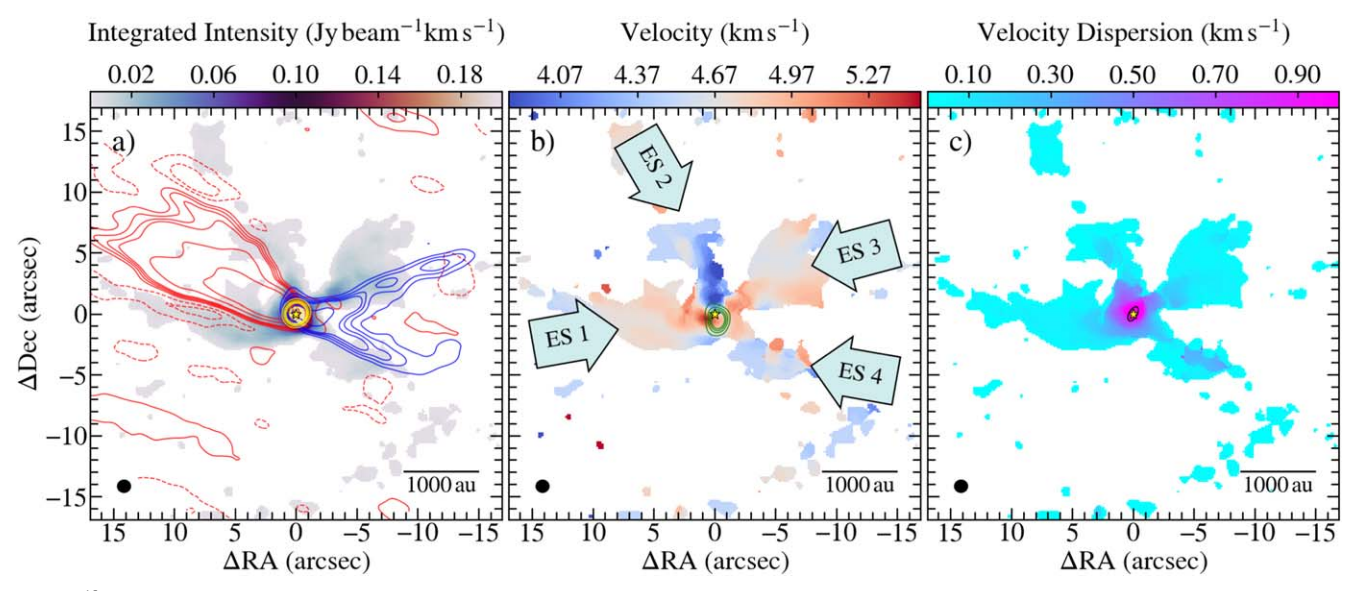


Figure 1.  $C^{18}O$  ( $J=2\to1$ ) integrated intensity (a), intensity-weighted velocity (b) and intensity-weighted velocity dispersion (c) maps. Red and blue contours represent the red and blueshifted outflows in  $^{12}CO$ , respectively, at levels of  $-10\sigma$ ,  $-5\sigma$ ,  $5\sigma$ ,  $10\sigma$ ,  $15\sigma$ ,  $20\sigma$ ,  $50\sigma$ , and  $100\sigma$ , where  $\sigma=22.35$  mJy beam $^{-1}$  km s $^{-1}$ . Yellow contours in the center show the 1.3 mm continuum emission at the same levels as  $^{12}CO$ , where  $\sigma=1.89$  mJy beam $^{-1}$ . Green contours represent the SO emission at the same levels as  $^{12}CO$ , where  $\sigma=2.40$  mJy beam $^{-1}$  km s $^{-1}$ . The yellow star denotes the position of Lupus 3-MMS. The arrows point to four extended structures (ES) of interest. All maps were made by excluding pixels under  $5\sigma$  from the image cube, where  $\sigma=3.47$  mJy beam $^{-1}$  channel $^{-1}$ .

Table 1
Summary of Image Results

		This Work		Yen et al. 2017		
Line/Continuum	Rest Frequency	Beam Size (PA)	$\sigma_{ m rms}$	Beam Size (PA)	$\sigma_{ m rms}$	
$C^{18}O\ (J=2\to 1)$	219.56035 GHz	1."10 × 1."04(86.81)	3.47	0."53 × 0."48(21°)	2.9	
SO $(J = 5_6 \rightarrow 4_5)$	219.94944 GHz	$1.10 \times 1.04(84.48)$	4.20	$0.753 \times 0.47(20^{\circ})$	3.5	
$^{12}CO (J = 2 \rightarrow 1)$	230.53800 GHz	$1.15 \times 1.04(-83.65)$	4.50	$0.751 \times 0.46(24^{\circ})$	2.5	
1.3 mm continuum	234.00000 GHz	$1.10 \times 1.04(-86.79)$	1.89	$0.49 \times 0.46(8^{\circ})$	0.2	

**Note.** Rest frequencies of the molecular lines are taken from the *Splatalogue* online database (https://splatalogue.online//). The noise level ( $\sigma_{rms}$ ) was calculated using channels 5–15 in each image cube and in an off-center region in the continuum image. The noise for the molecular line images is in units of mJy beam<sup>-1</sup> channel<sup>-1</sup>, while the noise for the continuum image is in units of mJy beam<sup>-1</sup>.

of 0."15 per pixel, and a velocity resolution of 0.1 km s<sup>-1</sup> and one continuum image, also with an image size of 320 pixels and a cellsize of 0."15 per pixel.

#### 3. Results

Table 1 shows a summary of our image results. The use of natural weighting with a UV taper produces images with a beam size of  $\sim$ 1". The shorter baselines in our data contain the flux from extended emission, which is crucial for our analysis. We compare to the image results obtained by Yen et al. (2017a), who cleaned the data using Briggs weighting and a robust parameter of +0.5 to achieve beam sizes of  $\sim$ 0".5. Their higher-resolution images are better suited toward resolving the Keplerian disk and analyzing its properties. As a note, we only show the  $^{12}\text{CO}$ , SO and 1.3 mm continuum results as contours, since our focus is mainly on the potential accretion flow tracer C18O; we will briefly describe their results in the order as they appear in the figures.

Figure 1 shows our C<sup>18</sup>O results of Lupus 3-MMS. We uncover four clear structures in C<sup>18</sup>O that extend out from the central region and follow the edges of the <sup>12</sup>CO outflow (Figure 1(a)). The structures appear to extend much further than previously noted by Yen et al. (2017a). Each is on the order of

a few thousand au in length. The bipolar outflow has two clear red and blueshifted components, shown as red and blueshifted contours (Figure 1(a)). The redshifted outflow appears to be straight, while the blueshifted component is slightly bent toward the north direction. The outflows were previously found to have position angles (PA) of 60°, 265° and inclination angles (i) of  $65^{\circ}$  and  $5^{\circ}$  for the red and blueshifted components, respectively. The 1.3 mm continuum emission in yellow contours shows a single compact structure with a central position of R. A.  $(J2000) = 16^{h}09^{m}18^{s}09$  and decl. (J2000)= -39d04m53. There is a clear velocity gradient in the central region showing the rotationally supported disk (Figure 1(b)). The SO emission in green contours also shows a compact structure slightly off-center from the source. We label our four extended structures (ES) with arrows. ES1 is a structure extending  $\sim 2000$  au under the redshifted outflow. The emission from ES1 is mostly redshifted in velocity and attaches to the redshifted part of the disk. Near the far end of the flow, the emission becomes slightly blueshifted. ES2 is a structure extending  $\sim$ 1300 au above the redshifted outflow. The emission from ES2, unlike the outflow, is blueshifted and has a higher velocity closer to the disk. ES3 is a structure extending  $\sim$ 1800 au above the blueshifted outflow. The

emission from ES3 seems to have a mixture of blue and redshifted velocities. ES4 is a structure extending  $\sim\!1600\,\mathrm{au}$  below the blueshifted outflow. The emission from ES4 also has a mixture of blue and redshifted velocities, with the outer part being more blue and the inner part turning to red. The velocity dispersion in the central region is high due to the faster Keplerian rotation of the disk. All of the extended structures have a relatively low level of velocity dispersion (<0.5 km s $^{-1}$ ), indicating that the gas is not being perturbed (Figure 1(c)). Except for the right edge of the redshifted outflow, we found the velocity dispersion to be>1.0 km s $^{-1}$  in the  $^{12}\text{CO}$  emission. This hints that the gas may not be affected by the outflow and could actually be a separate component, rather than just a part of the outflow cavity.

#### 4. Analysis

#### 4.1. The CMU Model

The CMU (Cassen-Moosman-Ulrich) model describes the infalling particle trajectories (or streamlines) around a point mass in the gravitational collapse of a rotating, spherically symmetric cloud (Ulrich 1976; Cassen & Moosman 1981; Chevalier 1983; Terebey et al. 1984). The assumptions of this model are:

- 1. The cloud is undergoing solid-body rotation at a uniform angular velocity  $(\Omega)$
- 2. The central star is treated as a point mass, meaning selfgravity of the envelope is not considered
- The particle starts from a spherical surface at a radius (r<sub>0</sub>)
  and follows a parabolic trajectory until it collides with
  the disk
- Specific angular momentum along the trajectory is conserved
- Pressure forces are negligible, meaning trajectories are ballistic (under the constraint that streamlines do not intersect)
- 6. Disk and envelope mass are not considered
- 7. Magnetic fields are not considered

Parabolic trajectories of the infalling matter are described by the trajectory equation:

$$r = \frac{j^2}{GM_*} \frac{1}{1 - \cos \nu},\tag{1}$$

where j is the specific angular momentum,  $M_*$  is the stellar mass, and  $\nu$  is the direction angle of the particle measured from the origin to apastron. Due to the spherical geometry of this model, we have the following angular relations:

$$\cos \theta = \cos \nu \cos \theta_0 \tag{2}$$

$$\tan \nu = \tan(\phi - \phi_0)\sin \theta_0,\tag{3}$$

where  $\theta_0$  is the polar angle of the orbital plane for the particle trajectory,  $\phi_0$  is the azimuthal angle of the orbital apastron, and  $\theta$  and  $\phi$  are the polar and azimuthal angles of the particle after a time t. The radius of the point at which the streamlines intersect with the disk  $(r_p;$  i.e., the semi-latus rectum of the parabolic trajectory) depends on the initial polar angle  $\theta_0$  and is described by

$$r_p = \frac{r_0^4 \Omega^2}{GM_{\odot}} \sin^2 \theta_0. \tag{4}$$

This equation is a result of angular momentum conservation. When  $\theta_0 = 90^{\circ}$ , the radius at which the particle collides with the disk is maximum. This is referred to as the centrifugal radius  $(r_c)$  and is described by

$$r_c = \frac{r_0^4 \Omega^2}{GM_*}. (5)$$

In a spherical rotating system, the specific angular momentum is expressed as

$$j^2 = r_0^4 \Omega^2 \sin^2 \theta_0.$$
(6)

Using Equation (2) and combining Equations (5) and (6), we can rewrite the trajectory equation as

$$\frac{r}{r_c} = \frac{\sin^2 \theta_0}{1 - \cos \theta / \cos \theta_0}. (7)$$

Equations (2), (3), and (7) lay the framework for the position of the particles in the CMU model. To complete the framework, we also need the velocity of the particles. In spherical coordinates, the CMU model describes the velocities as

$$v_r = -\left(\frac{GM_*}{r}\right)^{1/2} \left(1 + \frac{\cos\theta}{\cos\theta_0}\right)^{1/2} \tag{8}$$

$$v_{\theta} = \left(\frac{GM_*}{r}\right)^{1/2} \left(\frac{\cos\theta_0 - \cos\theta}{\sin\theta}\right) \left(1 + \frac{\cos\theta}{\cos\theta_0}\right)^{1/2} \tag{9}$$

$$v_{\phi} = \left(\frac{GM_*}{r}\right)^{1/2} \left(\frac{\sin\theta_0}{\sin\theta}\right) \left(1 - \frac{\cos\theta}{\cos\theta_0}\right)^{1/2}.$$
 (10)

In order to quantitatively compare to observations, the spherical geometry is easily converted to a Cartesian system where it can then be rotated using rotation matrices to match the PA and inclination angle (i) of the source. Figure 2 displays the CMU model plots. We are able to construct a 3D representation of the model, as well as make projections onto various axes and produce position–velocity (PV) diagrams. We take x and z to be the R.A. and decl. axes, and take  $v_y$  to be the line-of-sight velocity ( $v_{los}$ ). The observed velocity ( $v_{obs}$ ), which we can use to directly compare with our data, is then  $v_{sys} + v_{los}$ , where  $v_{sys}$  is the system velocity.

The CMU model describes trajectories infalling from everywhere in a globalized collapse scenario. It is possible that asymmetric density structures in the envelope cause overdensities in the infalling material that resemble stream-like structures (Tobin et al. 2012a). In this scenario, material may still be collapsing from everywhere around the disk, but only the overdense regions are visible in observations. We explore this idea more in Appendix A, where we test if various-sized patches of infalling particles can produce accretion streams. We find that streams can be produced in the different scenarios we tested. This supports the CMU model as a viable method to compare to accretion streams in observations.

#### 4.2. Disk Properties and System Velocity

Kinematic analysis is required in order to understand the nature of these extended structures. We need to ensure that the disk properties and system velocity are correct in order to effectively compare to our CMU model. Recently, Dzib et al. (2018) found a new distance to the Lupus III molecular cloud,

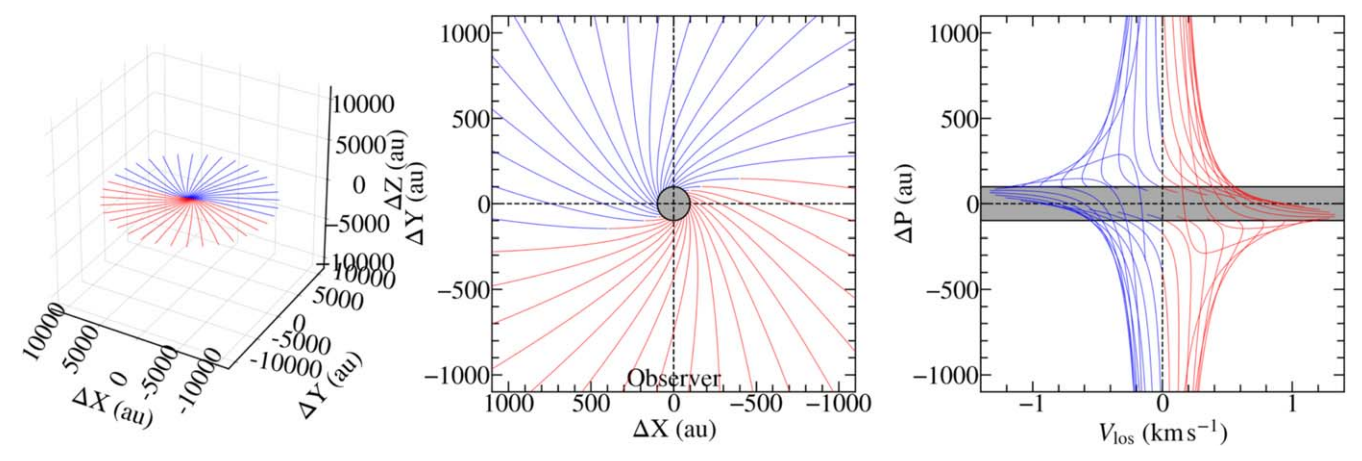


Figure 2. CMU model plots in 3D space (left), viewing the inner region from the top down (center) and the position–velocity structure in the inner region (right). In this example, we use  $M_* = 0.1 \, M_{\odot}$ ,  $r_c = 100$  au, and  $R_0 = 10,000$  au, with PA =  $90^{\circ}$  and  $i = 90^{\circ}$  for an edge-on disk configuration. For visualization purposes, we only plot streamlines at  $\theta_0 = 90^{\circ}$  (in the disk plane). The streamlines are blue or red depending on when the line-of-sight velocity ( $v_y$  in our model) is negative or positive. The gray areas mark the area within the centrifugal (disk) radius. The direction of the observer is also marked in the center plot. See Tobin et al. (2012a) for additional plots and information.

closer than that used by Yen et al. (2017a). Using Gaia DR2 data, they find a new distance of  $162 \pm 3$  pc. We adopt this new distance and scale the disk radius  $(r_d)$  and protostellar mass  $(M_*)$  previously derived from Keplerian rotation fitting. We use the original values of  $r_d=130$  au and  $M_*=0.3~\rm M_\odot$  to find scaled values of  $r_d^{\rm scaled}=105$  au and  $M_*^{\rm scaled}=0.24~\rm M_\odot$  at this new distance. In our model, we assume the value for  $r_d^{\text{scaled}}$  is equal to the centrifugal radius,  $r_c$ . Additionally, since our cubes were made with a slightly different velocity resolution and weighting than that used by Yen et al. (2017a), we refit the center of the C<sup>18</sup>O spectrum with a double peaked Gaussian to find a new centroid velocity  $(v_{sys})$  for comparing our model with observations. We chose a circular region with a radius of  $\sim 1''$  and extracted the spectrum from the image cube. Our fitting results give a new value of  $v_{\rm sys} = 4.67 \pm 0.59 \, {\rm km \, s}^{-1}$ . A correct value for  $v_{sys}$  is crucial for getting the correct observed velocity, though the value derived from kinematic fitting of the disk by Yen et al. (2017a) is within the margin for error.

#### 4.3. Outflow Velocity Structure

We do a number of comparisons between the  $C^{18}O$  emission that traces a number of extended features and the  $^{12}CO$  emission that traces the outflow. We first make PV cuts along the disk (PA =  $15^{\circ}$ ) and outflow (PA =  $6^{\circ}$ ) axis with two widths (0."5 and 20."0) to examine the velocity of the structures compared to the outflow. The PV cuts along the disk axis show that  $^{12}CO$  extends to much higher velocities, with the structures becoming much different in the wider 20."0 cut. The PV cuts along the outflow axis show very different velocity structures in both cuts, with the  $^{12}CO$  exhibiting a parabolic shape moving away from the center and increasing in velocity, while the  $C^{18}O$  emission is very centralized. These results are described in more detail and shown in Appendix B.

Instead, we make cuts along the disk axis at different points along the red and blueshifted outflows as another way to disentangle the outflow from the extended emission. The PA of the disk previously found by Yen et al. (2017a) is 150°. Figure 3 shows the positions of each cut overlaid on the C<sup>18</sup>O intensity-weighted velocity map (Figure 3, left) and each of their respective PV diagrams (Figure 3, right). For each PV cut, we plot the CMU model curves corresponding to a globalized

collapse scenario with  $\theta_0$  from  $30^\circ-150^\circ$  and  $\phi_0$  from  $0^\circ-360^\circ$ , both in steps of  $1^\circ$ , around a protostellar mass  $(M_*)$  of  $0.24\,\mathrm{M}_\odot$  with the centrifugal radius  $(r_c)$  set to be 105 au. We find the  $\mathrm{C}^{18}\mathrm{O}$  emission structure in the PV diagrams to be fairly consistent with the overall structure of the CMU model. The  $\mathrm{C}^{18}\mathrm{O}$  emission lies mostly within the extent of the model curves. As well, we find some gaps in the CMU model trajectories seen in the PV diagrams. The  $\mathrm{C}^{18}\mathrm{O}$  emission mostly avoids these gaps while staying within the extent of the model. The high-velocity  $\mathrm{C}^{18}\mathrm{O}$  only appears around the center. In contrast, the  $^{12}\mathrm{CO}$  emission structure is much higher-velocity in each of the PV cuts, and seems to become more circular in shape and increase in velocity as we move further away along the outflow axis. The two molecules are most certainly tracing different dynamics in this system.

#### 4.4. Infall Velocity Structure

Since the emission of the C<sup>18</sup>O emission shows the most disconnect with the <sup>12</sup>CO outflow emission, we begin by investigating these structures more directly and compare them to the CMU infall model. To do this, we use the same method as in Cheong (2018), who apply a "dendrogram" algorithm (Rosolowsky et al. 2008) to their data to pick out structures from their C<sup>18</sup>O image cube in position-position-velocity (PPV) space. The dendrogram algorithm works by using the brightest pixels in the image cube to construct a tree, then adding fainter and fainter pixels until a new local maximum is found and a new structure is created. These structures form the "leaves" of the tree and are then connected by "branches," which are pixels that are not local maxima. All of these structures eventually merge and create a tree. We input a number of parameters into the algorithm, including a minimum noise threshold for the tree ( $\sigma_{\min}$ ), a minimum significance for structures ( $\delta_{min}$ ), and the minimum number of pixels that a structure should contain in order to remain an independent structure  $(n_{\text{pix,min}})$ . We set  $\sigma_{\text{min}}$  to be  $2\sigma$ ,  $\delta_{\text{min}}$  to be  $7\sigma$ , and  $n_{\rm pix,min}$  to be 150 pixels. These parameters were decided by testing different values to find the set that showed the most coherent structures. We run the algorithm on our C<sup>18</sup>O image cube and find a total of eight structures. Figure 4 shows the dendrogram tree structure of our result. Out of these eight, only

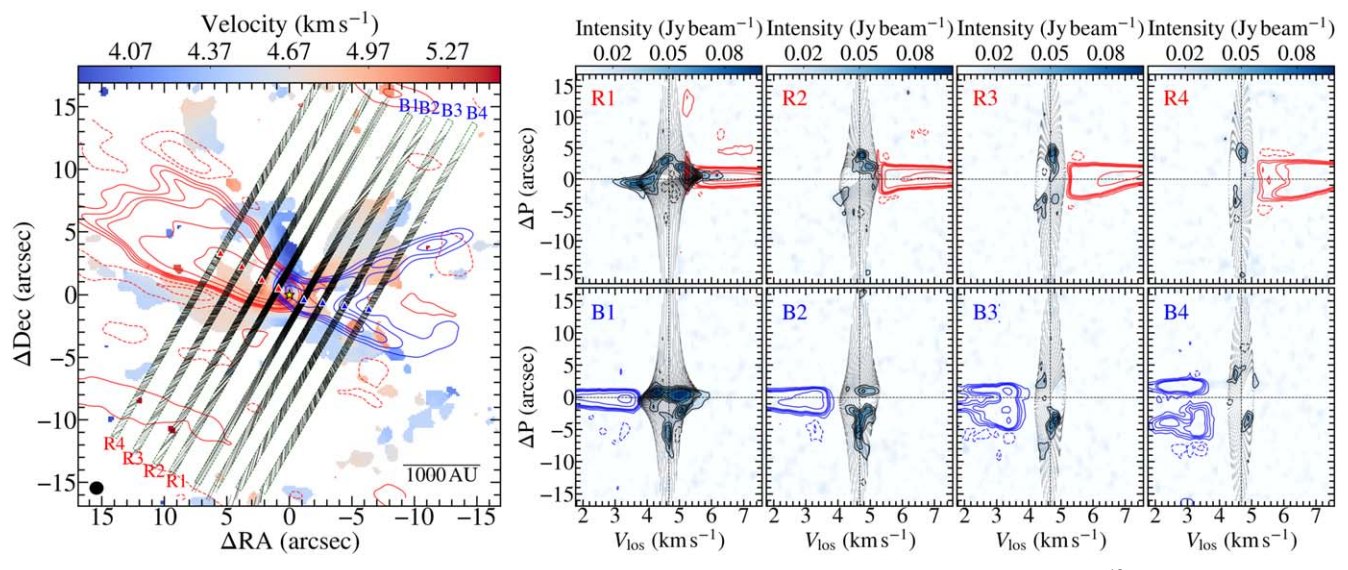
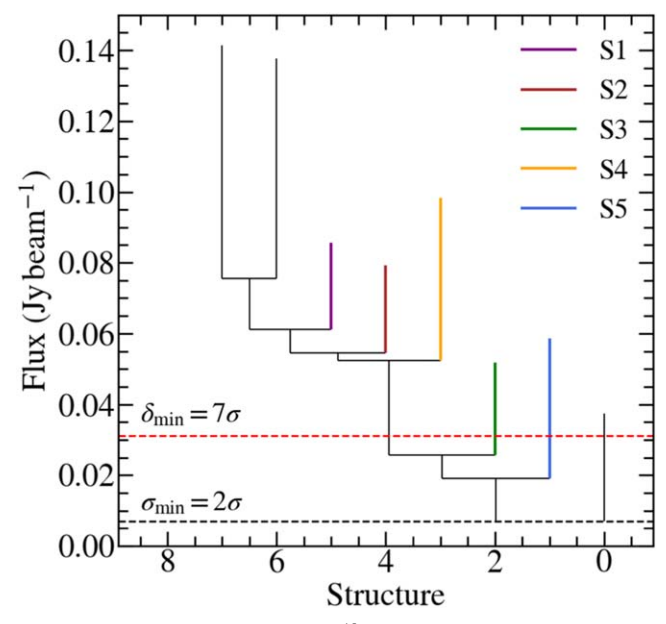


Figure 3. PV cuts using the disk PA taken at different points along each outflow axis. The positions of each cut are overlaid on the  $C^{18}O$  intensity-weighted velocity map and the  $^{12}CO$  integrated-intensity contours from Figure 1 (left). We plot the CMU model trajectories inside each cut (black lines) using  $\theta_0$  from  $30^{\circ}-150^{\circ}$  and  $\phi_0$  from  $0^{\circ}-360^{\circ}$ , both in steps of  $1^{\circ}$ . The colored triangles show the center of each cut. The PV diagrams for each cut (right) of  $C^{18}O$  (background and black contours) and  $^{12}CO$  (red and blue contours) show the cuts along the redshifted (right, top row) and blueshifted (bottom right) outflows, with distance increasing to the right. All contours show levels of  $-10\sigma$ ,  $-5\sigma$ ,  $5\sigma$ ,  $10\sigma$ ,  $15\sigma$ ,  $20\sigma$ ,  $50\sigma$ , and  $100\sigma$ , where  $\sigma(C^{18}O) = 3.37$ , 3.11, 3.03, 3.12, 3.13, 2.98, 3.39, and 3.16 mJy beam $^{-1}$ , and  $\sigma(^{12}CO) = 12.07$ , 13.65, 20.69, 21.02, 6.80, 7.34, 6.79, and 6.93 mJy beam $^{-1}$ , from left to right, top to bottom. The noise values were calculated from a square region in the bottom left corner of the PV image with no emission.



**Figure 4.** Dendrogram tree of our  $C^{18}O$  image cube. We label five leaf structures corresponding with our extended structures of interest, each labeled with a different color. We plot two horizontal lines for the minimum noise threshold  $(\sigma_{min})$  and the minimum significance for structures  $(\delta_{min})$ , where  $\sigma=3.47$  mJy beam $^{-1}$ .

five are correlated with the extended structures of interest we previously labeled in Figure 1.

We explore these structures in PPV space and compare their morphologies to the CMU model (Figure 5). Figure 5 (left) shows the 3D structures of our dendrograms and CMU model streamlines in PPV space. Figure 5 (center, right) decomposes the PPV space into position–position (PP) and PV spaces. We start by going through each structure and finding a CMU streamline that matches in both position and velocity to a pixel in the dendrogram structure. We set criteria for a point along

the CMU trajectory to match with a point in the PPV dendrogram structure. The point along the streamline must lie within the R.A. and decl. of the dendrogram point  $\pm$  half of the image cube pixel width and the line-of-sight velocity  $\pm$  half of the image cube velocity resolution. Our pixel size of 0."15 corresponds to  $\sim$ 24 au, and the velocity resolution was set to  $0.1 \,\mathrm{km \, s^{-1}}$ . Each streamline has an initial radius  $(r_0)$  of 10,000 au and ends at the centrifugal radius, which we assume is equal to the disk radius of 105 au. The mass of the central point source is taken to be  $0.24 M_{\odot}$ , i.e., the mass of the central protostar. We search for a streamline that has at least one matching point in each structure, then increase the range of the trajectory parameters ( $\theta_0$  and  $\phi_0$ ) angles until the number of matching points reaches a maximum. We use the maximum number of matching points divided by the number of points in the dendrogram to calculate a fitting percentage. This fitting percentage is to quantify how many pixels within the structure can be matched with the CMU model. We find most of our streams are consistent with the CMU model (Table 2). S1 and S2 match 100%, while S3 and S5 match >95%. S4 shows a large discrepancy, with a fit percentage of <30%, due to very low-velocity points (near the system velocity) seen in the PV diagram (Figure 5 right) between -3'' and -7''.

Using the matching points found from the CMU model (x, z, and  $v_y)$ , we can construct a representation in 3D position–position–position (PPP) space by taking the z coordinate at the same indices (Figure 6). Additionally, we plot the red- and blueshifted outflows using the parameters derived by Yen et al. (2017a). They adopt an axisymmetric wind-driven outflow model (Lee et al. 2000) and fit the position and inclination angles of the outflows. In PPP space, we see that the CMU points with a >95% fit seem to be infalling more in line with the disk plane, while S4 aligns more next to the edge of the outflow and shows large gaps of missing points along the flow. The flows are all found at different positions around the disk. S1 and S2 are both found close to each other, indicating that

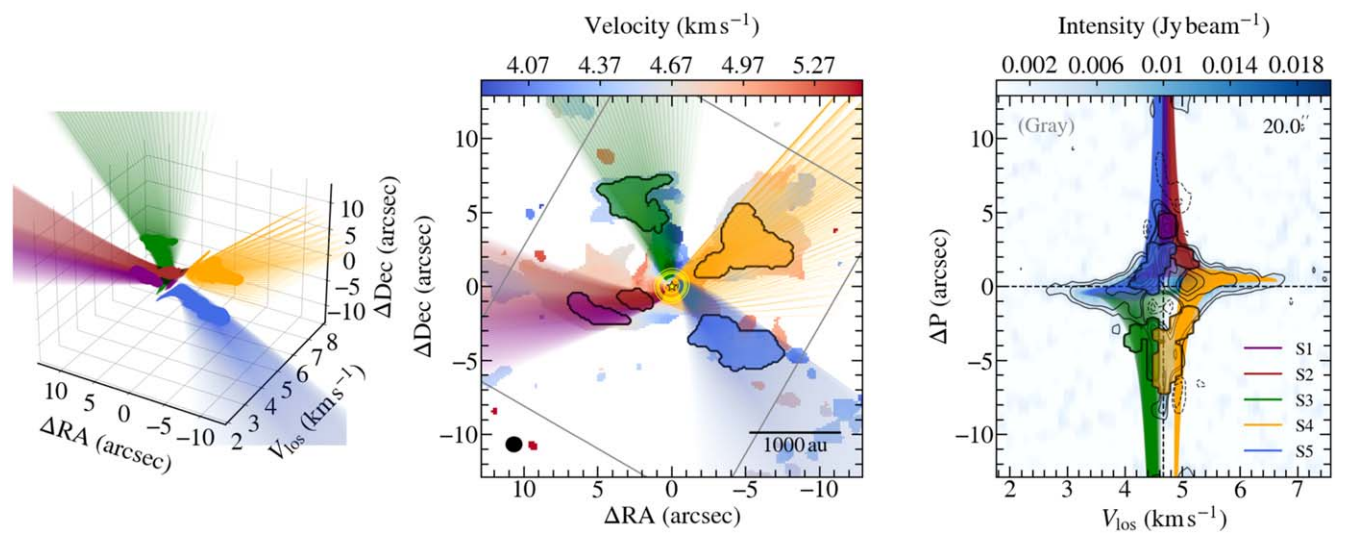


**Figure 5.** PPV matching of the CMU model to the dendrogram structures in three different views: PPV space (left), PP space (center), and PV space (right). The colors all correspond to the same structures found in Figure 4. The dendrogram structures are all shown as surfaces, while the trajectories from the CMU model are shown as streamlines. The gray box (center figure) shows the PV cut along the disk plane with a width of 20.10 C notours in the PV diagram show levels of  $-10\sigma$ ,  $-5\sigma$ ,  $-3\sigma$ ,  $3\sigma$ ,  $5\sigma$ ,  $10\sigma$ ,  $15\sigma$ ,  $20\sigma$ ,  $50\sigma$ , and  $100\sigma$ , where  $\sigma = 0.91$  mJy beam.

Table 2
Dendrogram Matching

Dendrogram Structure	r <sub>0</sub> (au)	$\theta_0$ Range (°)	$\phi_0$ Range (°)	# of Matching Points	# of Dendrogram Points	Fit Percentage
S1	10000	118–139	120–142	279	279	100%
S2	10000	111-128	90-116	157	157	100%
S3	10000	125-157	298-368	454	469	96.80%
S4	10000	50-58	52-77	359	1199	29.94%
S5	10000	31–74	201-252	1050	1060	99.06%

**Note.** The step size for both  $\theta_0$  and  $\phi_0$  is set to 1°. The fitting percentage is calculated from the number of matching points divided by the total number of points in the dendrogram.

they may actually be part of the same infalling structure but could not be identified as one in the dendrogram. S3 is falling from above the disk, while S5 is coming in from below. S4 is located almost completely along the line of sight and runs adjacent to the blueshifted outflow.

We derive several properties of our accretion flows using the matched 3D components of our model (Table 3). The distances are roughly similar in 2D space, ranging between 591 and 1416 au. The differences arise when the distance is calculated from the 3D coordinates. The largest discrepancy is more than 7000 au in S4 and is caused by the matching points being mainly along the line of sight. S5 is also slightly more along the line of sight, giving a discrepancy of  $\sim$ 520 au. S1, S2, and S3 are mostly in the plane of the sky, and only change by values of  $\sim$ 100 au or less. Next, we make C<sup>18</sup>O column density maps using the method from Mangum & Shirley (2015) in order to estimate the mass of each flow. We describe and show the column density maps for each structure in Appendix C. Summing the column density in each structure and assuming a  $C^{18}O$  abundance with respect to  $H_2$ ,  $[C^{18}O/H_2]$ , of  $1.7 \times 10^{-7}$ (Frerking et al. 1982), we estimate the flow masses to be between  $1.3-5.1 \times 10^{-3} M_{\odot}$ . We kinematically derive the infall timescale based on the lengths and infalling velocities of the flows, finding a range of  $1.5-9.8 \times 10^4$  yr. Using the flow mass and the infall timescale, we estimate the mass-infall rate of the flows to be  $0.5-1.1 \times 10^{-6} M_{\odot} \, \text{yr}^{-1}$ . The specific angular momentum along a trajectory is conserved, but can vary based on  $\theta_0$ . We combine Equations (4) and (5) to derive  $j=\sqrt{GM_*r_c}\sin\theta_0$ , and find values of  $\sim 10^{-4}\,\mathrm{km\,s^{-1}}\,\mathrm{pc}$ . Last, we use the specific angular momentum and multiply it by the flow mass in order to calculate the total angular momentum of each flow, getting values ranging from  $0.76-7.75\times10^{-6}\,M_\odot\,\mathrm{km\,s^{-1}}\,\mathrm{pc}$ .

#### 5. Discussion

#### 5.1. Outflow Cavities or Accretion Flows?

We aimed to disentangle whether the extended emissions in Lupus 3-MMS are part of the outflow cavity or are accretion flows. Outflow cavities are thought to be formed by a wind driven from the circumstellar disk of a protostar that pushes gas toward the outer edges of the outflow. This leads to questions such as whether the material in the outflow cavity has a velocity structure similar to that of the outflow, whether material can be recycled from the outflow and accrete back onto the disk, or if large-scale material can fall along the outflow cavities. Comparing the velocity structures of the extended structures and the outflow velocity structure yields almost no similarities. First, the velocity dispersion in the extended structures is low compared to that at the center (Figure 1(c)). One might expect the velocity in the outflow cavities to be perturbed if they were being influenced by the

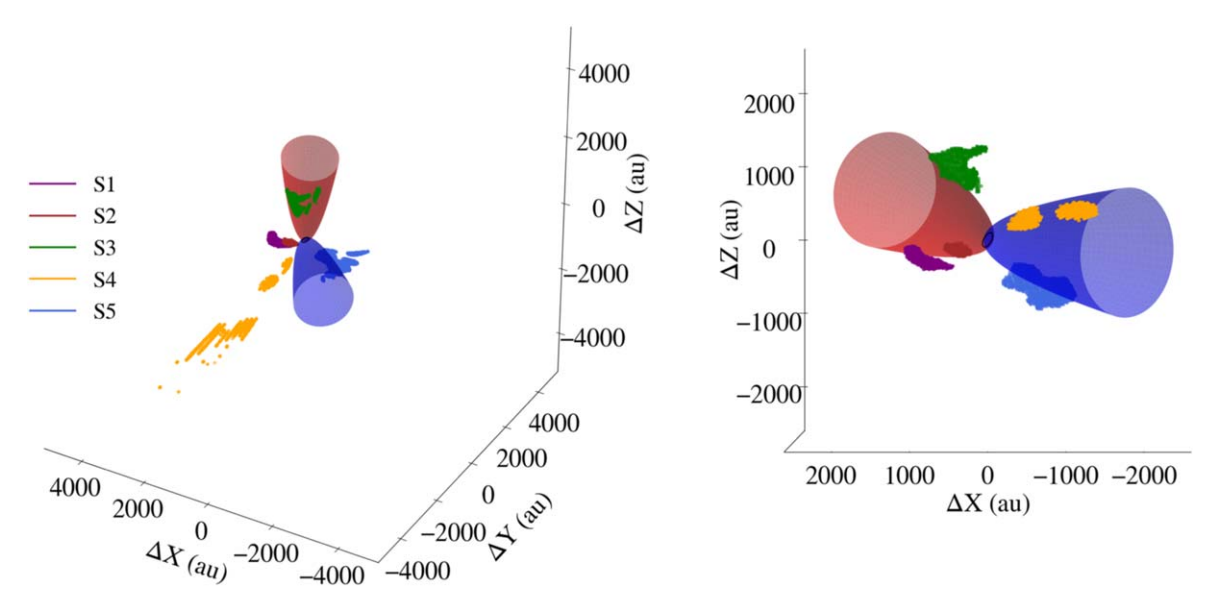


**Figure 6.** PPP trajectories using the matched points from the CMU model. The x- and z-axes correspond to the R.A. and decl., while the y-axis is the line-of-sight axis. The colored dots all correspond to the same colored structures found in Figure 4. The red and blue cones represent the red and blueshifted outflows using the position and inclination angles derived by Yen et al. (2017a). An animation of this figure is available, where it is rotated about the z-axis. The sequence repeats three times and the real-time duration of the animation is 42 s.

(An animation of this figure is available.)

Table 3
Accretion Flow Properties

Dendrogram Structure	r <sub>max,2D</sub> (au)	r <sub>max,3D</sub> (au)	N (cm <sup>-2</sup> )	$M_{ m flow} \ ({ m M}_{\odot})$	t <sub>infall</sub> (yr)	$(M_{\odot} \text{ yr}^{-1})$	$(\text{km s}^{-1}\text{pc})$	$\frac{J}{(M_{\odot} \mathrm{km  s}^{-1} \mathrm{pc})}$
S1 S2 S3 S4 S5	1128 591 1349 1367 1416	1130 610 1460 8480 1940	$2.38 \times 10^{13}$ $1.24 \times 10^{13}$ $2.01 \times 10^{13}$ $9.39 \times 10^{13}$ $3.80 \times 10^{13}$	$3.20 \times 10^{-3}$ $1.67 \times 10^{-3}$ $2.69 \times 10^{-3}$ $1.26 \times 10^{-2}$ $5.09 \times 10^{-3}$	$3.55 \times 10^{3}$ $1.54 \times 10^{3}$ $5.51 \times 10^{3}$ $2.25 \times 10^{5}$ $9.81 \times 10^{3}$	$9.01 \times 10^{-7}$ $1.06 \times 10^{-6}$ $4.88 \times 10^{-7}$ $5.60 \times 10^{-8}$ $5.19 \times 10^{-7}$	$4.76-6.40 \times 10^{-4}$ $5.71-6.77 \times 10^{-4}$ $2.83-5.94 \times 10^{-4}$ $5.55-6.15 \times 10^{-4}$ $3.73-6.97 \times 10^{-4}$	$1.52-2.05 \times 10^{-6}$ $0.95-1.13 \times 10^{-6}$ $0.76-1.60 \times 10^{-6}$ $6.99-7.75 \times 10^{-6}$ $1.90-3.55 \times 10^{-6}$

**Notes.** The maximum 2D radius ( $r_{\text{max},2D}$ ) is calculated from the maximum X and Z model values matching with the dendrogram structure, while the maximum 3D radius ( $r_{\text{max},3D}$ ) is calculated from the maximum X and Z and the corresponding Y model values. The column density (N) totals are assuming C<sup>18</sup>O excitation temperatures of 30 K. The mass of the flows ( $M_{\text{flow}}$ ) is the H<sub>2</sub> mass, while the infall timescale ( $t_{\text{infall}}$ ) is calculated kinematically, based on the lengths and velocities of the flows. The mass-infall rate ( $\dot{M}_{\text{infall}}$ ) is calculated using the mass of the flows and the infall timescale. The specific angular momentum (j) values are the min-max values corresponding to the model positions matched with the dendrogram structures, where the total angular momentum (J) is found by multiplying by the flow mass.

outflow. Furthermore, the velocity along the <sup>12</sup>CO outflows is much higher than what is seen in C<sup>18</sup>O. If the material in the extended structures is really being pushed by the outflow, then for a given momentum input, we expect the lower-density outer part should show a higher velocity. We do not expect missing flux to affect this point, as any high-velocity components should still be captured by our observations. Comparing with the globalized CMU model shows the C<sup>18</sup>O emission to stay within the extent of the model and avoids the holes seen in the PV diagrams. This seems to indicate that the structures are infalling. Further comparisons with the CMU model were made by isolating structures in PPV space using a dendrogram algorithm, to confirm that these structures are infalling accretion flows. S1, S2, S3, and S5 match the CMU model in PPV space with >95% fits. S1 and S2 show remarkable similarity, with fittings of 100%. It could be that these two are in fact part of the same structure, due to their proximity in position space, but are separated into two structures due to missing flux. Follow-up observations with shorter baselines are needed to test this. S3 and S5 have more than twice as many pixels as the former two while still retaining high fitting percentages of 96.80% and 99.06%, respectively. Thus, these structures in C<sup>18</sup>O can be better explained with an infall model and cannot be explained with an outflow model. Another sign that accretion is taking place is the presence of a small patch of SO near the redshifted part of the disk (Figure 1(b)). The presence of SO is thought to be an indication of accretion shocks (Sakai et al. 2014). Since SO only shows a blueshifted component on one side of the disk, this could be an indication of asymmetric accretion.

#### 5.2. The Nature of S4

S4 has the lowest fitting percentage of less than 30% from our CMU matching. S4 shows a much lower velocity component in the PV diagram (Figure 5, right). We explored whether the material was further away from the protostar along the same trajectories. To test this, we increased the initial radius of the particle  $r_0$  from 10,000 au (i.e., the typical dense core size of  $\sim$ 0.1 pc) out to 20,000 au (i.e., twice the typical core size). The CMU model traces the trajectory of the particle merely due to the gravitational pull of the central point mass.

 Table 4

 Comparison with Previously Observed Accretion Flows

Source Name	Class	r <sub>flow</sub> (au)	$(\text{km s}^{-1}\text{pc})$	$M_{ m flow} \ ({ m M}_{\odot}$ )	t <sub>acc</sub> (yr)	$(\mathrm{M_{\odot}yr^{-1}})$	References
Lupus 3-MMS	0	591-1416	$2.8 - 7.0 \times 10^{-4}$	$1.7 - 5.1 \times 10^{-3}$	$1.5 - 9.8 \times 10^3$	$0.5 - 1.1 \times 10^{-6}$	1
VLA 1623	0	1200-3600	$1.0 - 1.5 \times 10^{-3}$	$2.7 - 6.4 \times 10^{-3}$	$4.4 - 8.7 \times 10^3$	$1.2 \times 10^{-6}$	2
IRAS 03292+3039	0	10,500		0.1	$9.6 \times 10^{4}$	$1 \times 10^{-6}$	3
L1489-IRS	I	2000-5000	$4.8 \times 10^{-3}$	$4-7\times10^{-3}$	$3-5\times10^{4}$	$4-7\times10^{-7}$	4
HL Tau	I	1000-2000	$1.9 \times 10^{-3}$	$5.7 \times 10^{-3}$	$2.6 \times 10^{3}$	$2.2 \times 10^{-6}$	5

**Note.** The values listed for Lupus 3-MMS are only from the accretion flows with a fitting percentage >95%. The radius of the accretion flow ( $r_{flow}$ ) is the projected 2D radius on the plane of the sky.

References. (1) This work; (2) Cheong 2018; (3) Pineda et al. 2020; (4) Yen et al. 2014; (5) Yen et al. 2017b.

Increasing the distance would allow for lower-velocity components along the trajectory. We reran the same fitting procedure as in Section 4.4, only to find the fitting percentage to increase from 29.94% to 30.03%, an increase of less than 1%. Adjusting  $\theta_0$  and  $\phi_0$  also had no effect on this scenario. It is unlikely the unfit components are due to material that is further away along the line-of-sight. Additionally, material so far away runs into the issue of also being resolved out by the ALMA 12 m array.

We considered whether or not the material could be affected by magnetic braking. Recently, numerical simulations of protoplanetary disk formation by Lee et al. (2021) found that, in their simulations, material falling closer to the disk plane experienced more freefall motion, while material falling closer to the outflow and the cavity was more prone to magnetic braking (see Figure 20 in their paper). S4 is located mainly along the line of sight toward the observer direction next to the blueshifted outflow (Figure 6). If the low fitting percentage of S4 was due to magnetic braking, we might also expect S3 and S5 to have lower fitting percentages as well, as they show some components that are located positionally close to the outflow. This scenario would need to be tested against MHD simulations in order to confirm this possibility, which is beyond the scope of this paper.

The material along the streamline could be affected by the outflow. As we mentioned earlier, the velocity dispersion in each of the extended structures exhibits low, subsonic values. If the extended structures were being affected by the outflows, we would expect some kind of velocity perturbations due to the energetic outflowing material. It is not likely that this stream is being affected by the outflow.

Missing flux at low velocities can bias the mean velocities away from the systemic velocity (Yen et al. 2017b). This could explain why there is a low-velocity component that is not fit by the streamline model. S4 is found to go out to  $\sim$ 8000 au in 3D space, making it longer than the other streams and more likely to have missing flux at these larger scales.

Another quality of S4 is that it seems to have gaps in the fitting along the streamline. This could be due to the physical and chemical structure inside the envelope, causing different excitation conditions along the streamline. It may be possible that portions of the accretion flows are traced by different molecules, just as in HL Tau (Yen et al. 2017b, 2019), where accretion flows are traced in <sup>13</sup>CO and HCO<sup>+</sup>. Thus, the gaps may be observable in other molecules or transitions.

#### 5.3. Degeneracy of the CMU Model

The CMU model has four key parameters: stellar mass  $(M_*)$ , centrifugal radius  $(r_c)$ , trajectory inclination  $(\theta_0)$ , and azimuthal

angle of apastron ( $\phi_0$ ). Various combinations of these properties could potentially lead to the same outcome in the fitting percentage calculated in Section 4.4. We test this by rerunning our fitting calculations using the star  $(0.24 \, M_{\odot})$  + disk  $(0.1 \, M_{\odot})$  mass and finding new ranges for  $\theta_0$  and  $\phi_0$ . For the disk mass, we use the value derived by Yen et al. (2017a). For S1, we can still get 100% fitting by only changing the mass while keeping the same  $\theta_0$  and  $\phi_0$  range. For S2, we can change the range of  $\theta_0$  from 111°-129° to 112°-131° and  $\phi_0$  from 90°-117° to 92°–119°. Doing this, we can achieve a fitting of 100%, like before. For S3, we can actually increase the fitting percentage from 96.80% to 100% by adjusting the range of  $\theta_0$ from  $125^{\circ}-157^{\circ}$  to  $123^{\circ}-155^{\circ}$  and  $\phi_0$  from  $298^{\circ}-368^{\circ}$  to  $316^{\circ}-$ 373°. For S4, the fitting percentage decreases from 29.94% to 24.85%. This is because adding more mass in the center increases the velocity along the trajectories, thus increasing the line-of-sight velocity in our model, and ends up with fitting less of the lower velocity points. Adjusting the range of  $\theta_0$  and  $\phi_0$ had no affect on this value. For S5, we can change the range of  $\theta_0$  from 31°-74° to 32°-81° and  $\phi_0$  from 201°-252° to 190°-252°. This increases the fitting percentage from 99.06% to 99.15%.

Tachihara et al. (2007) estimate the mass enclosed within 4200 au of Lupus 3-MMS to be  $0.52 M_{\odot}$ . Therefore, we also test the extreme case by running the model using the star  $(0.24\,M_\odot)$  + envelope  $(0.52\,M_\odot)$  mass and again finding new ranges for  $\theta_0$  and  $\phi_0$ . We find that we can achieve a 100% fit for all the structures, with the exception of S4, which we could only achieve a 7.59% fit. Again, the low fitting percentage of S4 is due to the larger mass increasing the velocity along the trajectories, which cannot fit the low-velocity part of the structure. We find the  $\theta_0$  and  $\phi_0$  ranges to be the same as before for S1, 117°-135° and 98°-125° for S2, 119°-150° and 338°- $381^{\circ}$  for S3, and  $34^{\circ}$ – $58^{\circ}$  and  $195^{\circ}$ – $253^{\circ}$  for S5. Our test show that values of  $M_*$  between 0.24  $M_{\odot}$  and 0.76  $M_{\odot}$  still find good solutions with the CMU model. This highlights that the overall results are not so sensitive to  $M_*$  when trying to match the trajectories.

#### 5.4. Accretion Flow Properties and Comparison

Our analyses indicate the presence of at least four clear accretion flows that match with the CMU model, the most to be found in any source to date. In Table 3, we derived several properties of the accretion flows found in Lupus 3-MMS. Here, we discuss these properties and compare them with previously observed accretion flows. Previous observations find accretion flows to be either singular (asymmetric) or bilaterally symmetric. To date, there are the only four sources (L1489-

IRS, HL Tau, VLA 1623, and IRAS 03292+3039) with observed accretion flow structures. Table 4 shows a summary of previously observed accretion flows. In this section, we discuss the various parameters and compare them to other sources. When comparing these other sources to Lupus 3-MMS, we will only compare to values in the structures that fit >95% with the CMU model.

#### 5.4.1. Flow Mass

The mass of the accretion flow  $(M_{flow})$  quantifies the reservoir of material available to feed the protostellar disk. This value is given as the H<sub>2</sub> flow mass, as it is the most abundant molecule. It is calculated by using the column density maps and the area of the structure estimated by the pixel area and the number of pixels. We then assumed an abundance ratio between C<sup>18</sup>O and H<sub>2</sub>, then multiplied by the H<sub>2</sub> mass to approximate the mass of the entire flow structure. We estimate the values in Lupus 3-MMS to be  $1.3-5.1 \times 10^{-3} M_{\odot}$ . The order of  $\times 10^{-3} M_{\odot}$  is overall comparable to the derivations in other accretion flows. It is most similar to VLA 1623, which shows slightly higher values of  $2.7-6.4 \times 10^{-3} M_{\odot}$ , also using C<sup>18</sup>O. There is a discrepancy between Lupus 3-MMS and IRAS 03292+3039, where Pineda et al. (2020) find a huge flow mass of  $0.1 M_{\odot}$ . This difference comes from the length of their flow being much longer, meaning the area of the flow is larger. In the two Class I sources, L1489-IRS and HL Tau, the masses are on the higher end, compared to Lupus 3-MMS, due to the similarities in lengths, but overall they are still consistent.

#### 5.4.2. Infall Timescale

The infall timescale  $(t_{infall})$  measures how long it will take the material in the flow to reach the disk. This value should be consistent with timescales shorter than that of protostellar evolution, which for low-mass protostars lasts roughly  $1.6 \times 10^5$  yr for the Class 0 phase (Evans et al. 2009). This value is estimated kinematically using the lengths of the flows and their velocities. We estimate values on the order of  $10^3$  yr in Lupus 3-MMS. Again, this is comparable to VLA 1623, which was calculated to be  $4.4-8.7 \times 10^3$  yr. In contrast, Pineda et al. (2020) estimate the infall timescale in IRAS 03292 +3039 using a different method based on the freefall timescale  $(t_{\rm ff})$ , which depends on the radius of the envelope and the mass enclosed within that radius. We use the mass enclosed derived by Tachihara et al. (2007), a value of  $0.52 M_{\odot}$ . Their value is estimated to be much higher due to the higher envelope mass and larger radius. We estimate the freefall timescale in Lupus 3-MMS to compare with IRAS 03292+3039 and the values derived kinematically. Using the same method as in Pineda et al. (2020), we calculate  $t_{\rm ff}$  to be  $6.01 \times 10^4$  yr, comparable to the value of  $9.6 \times 10^4$  yr for IRAS 03292+3039. L1489-IRS is on an order of magnitude of  $\sim 10^4$  yr, while HL Tau is  $\sim 10^3$  yr. The infall timescale is similar in these sources and may be reflected by the initial size-scale of the envelope.

#### 5.4.3. Mass-infall Rate

The mass-infall rate ( $\dot{M}_{\rm infall}$ ) assesses the rate at which material falls onto the protostellar disk from the infalling accretion flows. This value is estimated by dividing the mass of the flows with the infall timescale. For the Class 0 sources, these values are comparable, all around  $\sim \! 10^{-6} \, M_{\odot} \, {\rm yr}^{-1}$ . For the Class I sources, it varies from  $10^{-7} \, M_{\odot} \, {\rm yr}^{-1}$  to  $10^{-6} \, M_{\odot} \, {\rm yr}^{-1}$  in

L1489-IRS and HL Tau, respectively. One reason the massinfall rate may vary between sources is due to the remaining envelope mass. Sources with more envelope mass are expected to be accreting more material, and vice versa. From the Class I sample, envelope masses were derived from IRAM 30 m dust continuum observations to be  $0.03 M_{\odot}$  and  $0.13 M_{\odot}$  for L1489-IRS and HL Tau at 4200 au, respectively (Motte & André 2001). This explains the discrepancy between the accretion rates in the two Class I sources, as HL Tau has a much higher value. In Lupus 3-MMS, we previously mentioned this value was derived to be  $0.52 M_{\odot}$  at 4200 au. The envelope mass is substantially larger due to the younger nature of our source. In VLA 1623, Murillo et al. (2018) derive an envelope mass of  $\sim 1.0 \, M_{\odot}$ , assuming the two binary sources A & B share the same envelope. Pineda et al. (2020) cite a dense core mass of  $3.2 M_{\odot}$ for IRAS 03292+3039, the largest of all the sources. The higher mass-infall rates in the Class 0 sources all have much higher envelope masses, and the lower envelope mass in L1489-IRS has a lower mass-infall rate. Assuming the previously derived envelope mass in Lupus 3-MMS and a constant accretion rate, it will take around  $10^6$  yr to deplete the remaining envelope mass.

The mass-infall rate of  $\sim 1.53 \times 10^{-6} M_{\odot} \text{ yr}^{-1}$  for a 10 K singular isothermal sphere (Shu 1977) is consistent with the values derived for Lupus 3-MMS. In the context of numerical simulations, most show the presence of extended accretion flow structures (e.g., Li et al. 2014; Seifried et al. 2015). In more complicated MHD simulations, only a handful derive the mass-infall rate from the envelope to the disk. Machida et al. (2016) study the formation of the circumstellar disk in strongly magnetized cores. They derive mass-infall rates of  $\sim 10^{-5} M_{\odot} \,\mathrm{yr}^{-1}$ . Lee et al. (2021) study disk formation in a magnetized core with ambipolar diffusion. They find massinfall rates onto the disk to be  $\sim 10^{-6}\,M_\odot\,{\rm yr}^{-1}$  at both 40 and 80 kyr after the formation of the sink particle. One difference between these two simulations was the inclusion of ambipolar diffusion in the latter, which helps to reduce the efficiency of magnetic braking in the envelope. Our model does not include magnetic fields, but the mass-infall rate is still roughly consistent. Magnetic field observations are needed to carry out a more robust comparison with MHD simulations.

### 5.4.4. Specific Angular Momentum

Angular momentum is important for the formation of the protostellar disk in the earliest stages of star formation. The values we calculate for the specific angular momentum (j) of the accretion flows in Lupus 3-MMS are on the order of  $10^{-4} \,\mathrm{km \, s^{-1}} \,\mathrm{pc}$ . The specific angular momentum at the edge of the rotationally supported disk can be defined as the specific angular momentum of trajectories lying on the disk plane  $(j_d = \sqrt{GM_*r_d} = \sqrt{GM_*r_c} \sin \theta_0 \text{ as } \theta_0 = 90^\circ; \text{ see Equations (5)}$  and (6)), with a value of  $7.25 \times 10^{-4} \,\mathrm{km \, s^{-1}} \,\mathrm{pc}$ . Compared to other accretion flows, which show j on the order of  $10^{-3} \,\mathrm{km \, s^{-1} \, pc}$ , the specific angular momentum in Lupus 3-MMS is roughly an order of magnitude lower. This is due to the low stellar mass of  $0.24 M_{\odot}$ , compared to other sources that are more evolved into the Class I stage (L1489-IRS and HL Tau), binary systems where both of the sources are used for the estimation (VLA 1623), and a Class 0 where they use the envelope mass in their model calculation (IRAS 03292+3039). As the protostellar mass increases over time, the angular momentum would also increase. This could suggest Lupus 3-MMS is in the early stages of collapse. In comparison to other studies of the specific angular momentum in Class 0 sources, our results are consistent. Pineda et al. (2019) find specific angular momentum values to be between  $10^{-4}$ – $10^{-3}$  km s<sup>-1</sup> pc at distances less than 3000 au. Additionally, Gaudel et al. (2020) find the specific angular momenta of seven out of eight Class 0 sources to be 2– $7 \times 10^{-4}$  km s<sup>-1</sup> pc.

#### 5.4.5. Total Angular Momentum Budget

Estimating the total angular momentum (J) that will be delivered to the disk is another way to assess the material being fed to disk scales. We take the specific angular momentum of each flow and multiply it by the respective flow mass in order to calculate a range for each structure. If we add up the total angular momentum of each of the accretion flows, we find the total angular momentum in the process of being delivered to the disk to be  $1.21-1.61 \times$  $10^{-5} M_{\odot} \,\mathrm{km \, s^{-1} \, pc}$ . We then calculate the total angular momentum in the disk by taking its specific angular momentum and multiplying it by disk mass (0.1  $M_{\odot}$ , per Yen et al. 2017a) to get a value of  $7.25 \times 10^{-5} M_{\odot} \,\mathrm{km \, s^{-1}} \,\mathrm{pc}$ . This is slightly less than that of the disk, but on the same order of magnitude. As a check, we also calculate the total angular momentum assuming a disk surface density distribution (Williams & Cieza 2011). From this method, we find that the total angular momentum of the disk is  $\sim 1.00 \times 10^{-5} \, M_{\odot} \, \mathrm{km \, s^{-1}} \, \mathrm{pc}$ . The similarity in total angular momentum between the disk and accretion flows may hint that the disk is relatively young and has not had enough time to inherit more angular momentum from the parent envelope. Whether the angular momentum of the infalling-rotating envelope can be delivered all the way to the disk depends on the degree of magnetic braking, which can in principle remove angular momentum efficiently (e.g., Mellon & Li 2008). Dust polarization observations toward this object are needed in order to understand the magnetic field morphology and strength, which would be useful in understanding the role of magnetic braking in this object. Some angular momentum can also be removed by the protostellar outflows, but we do not have clear detection of outflow rotation in our current data. If material is falling in from everywhere around the disk, and the flows we detect are just overdensities of that material, then missing flux from shorter baselines could also potentially increase the amount of angular momentum being delivered to the disk.

#### 5.5. The Origin of Accretion Flows

Observations of different molecules give us an insight into where the accretion flows originate. Pineda et al. (2020) find their 10,500 au asymmetric accretion flow structure is traced by the "chemically fresh" carbon-chain molecules  $HC_3N$ , CCS, and  $^{13}CS$ , and not by more chemically evolved molecules like  $N_2H^+$  or  $N_2D^+$  (Bergin & Tafalla 2007; Sakai & Yamamoto 2013). They conclude from this that the material comes from beyond the parental denser core (>10,000 au). As for Lupus 3-MMS, the flows are traced by  $C^{18}O$ , a molecule present throughout the star formation process.  $N_2D^+$  was observed but not detected in these archival observations. In order to accurately assess the possible chemical complexity of these flows, observations of other fresh and evolved molecules are needed. Additionally, throughout this paper we have seen that the addition of shorter baseline observations could help fill

in the missing flux to further investigate the size and structure of the accretion flows on larger scales. Therefore, the present data are insufficient to allow us to conclude whether these structures originate from the dense core or from beyond.

#### 6. Conclusion

Identifying accretion flows is difficult, but important for characterizing how material is transported to the protostellar disk. We have reanalyzed ALMA archival observations of a young Class 0 protostar, Lupus 3-MMS, in  $C^{18}O$  ( $J=2\rightarrow1$ ),  $^{12}CO$  ( $J=2\rightarrow1$ ), SO ( $J=5_6\rightarrow4_5$ ), and 1.3 mm continuum emission. We uncover the dynamics of several accretion flows using the CMU model and demonstrate a case where accretion flows are hiding in the so-called "outflow cavity." The main results are summarized as follows:

- 1. We identify extended accretion flow-like structures in C<sup>18</sup>O along the sides of the red- and blueshifted <sup>12</sup>CO outflows after recleaning the data with a larger beam size. The extended structures range in lengths of 5"-15", while showing various line-of-sight velocity components and low-velocity dispersion. The disk is found in the central region, as indicated by the high-velocity C<sup>18</sup>O red and blueshifted components corresponding with the continuum emission and high-velocity dispersion. The SO emission near the disks indicates the possible presence of accretion shocks.
- 2. Comparing the velocity of the extended C<sup>18</sup>O structure with the outflow emission yields no similarities in PV space. Making cuts in the disk plane at different points along the outflows and comparing with a globalized case of our CMU model shows the C<sup>18</sup>O emission to match well with our infalling model curves, while the outflow shifts to higher velocities at greater distances from the source. These different dynamics are important for disentangling emission between the outflows and infalling gas.
- 3. Based on our dendrogram analysis of five coherent components within the extended structures, we identify four structures to be accretion flows that fit remarkably well with the CMU model, with fitting percentages of 95%. We translate the matching points from PPV space to PPP space and find that the accretion flows are separated from the outflow in 3D space. This highlights that studying emission near the outflow cavities is important for understanding the dynamics in young protostellar systems.
- 4. Using the matching points of these four structures, we derive specific angular momenta of  $2.8-7.0 \times 10^{-4}\,\mathrm{km\,s^{-1}}$  pc, column densities of  $1.2-3.8 \times 10^{-12}\,\mathrm{cm^{-2}}$ , flow masses of  $1.7-5.1 \times 10^{-3}\,M_\odot$ , infall timescales of  $1.5-9.8 \times 10^3\,\mathrm{yr}$ , and mass-infall rates of  $0.5-1.1 \times 10^{-6}\,M_\odot\,\mathrm{yr^{-1}}$ . We find that Lupus 3-MMS is comparable to other Class 0 sources with detected accretion flows. The higher mass-infall rates in the Class 0 sources show the importance of accretion at this phase, when the object is still highly embedded in its parent envelope. The mass-infall rate is comparable to MHD simulations, indicating that such a simplified model can be a good approximation to compare to observations.

We thank the anonymous referee for constructive comments that improved the clarity of this paper. T.J.T. and S.-P.L.

acknowledge support from the Ministry of Science and Technology of Taiwan via grants MOST 106-2119-M-007-021-MY3 and MOST 109-2112-M-007-010-MY3. C.-F.L. acknowledges grants from the Ministry of Science and Technology of Taiwan (MoST 107-2119-M-001-040-MY3) and the Academia Sinica (Investigator Award AS-IA-108-M01). H.-W.Y. acknowledges support from MOST 108-2112-M-001-003-MY2 and MOST 110-2628-M-001-003-MY3. Z.-Y.L. is supported in part by NASA 80NSSC20K0533 and NSF AST-1716259. This work used high-performance computing facilities operated by the Center for Informatics and Computation in Astronomy (CICA) at National Tsing Hua University. This equipment was funded by the Ministry of Education of Taiwan, the Ministry of Science and Technology of Taiwan, and National Tsing Hua University. This paper makes use of the following ALMA data: ADS/JAO.ALMA#2013.0.00879. S. ALMA is a partnership of ESO (representing its member states), NSF (USA) and NINS (Japan), together with NRC (Canada), MOST and ASIAA (Taiwan), and KASI (Republic of Korea), in cooperation with the Republic of Chile. The Joint ALMA Observatory is operated by ESO, AUI/NRAO, and NAOJ.

Facility: ALMA.

Software: Astropy (Astropy Collaboration et al. 2013, 2018, http://astropy.org), Astrodendro (Rosolowsky et al. 2008; Robitaille et al. 2019, http://dendrograms.org/), CASA (v5.1.2+4.6.2, McMullin et al. 2007, http://casa.nrao.edu/),

Matplotlib (Hunter 2007, http://matplotlib.org/), Numpy (van der Walt et al. 2011, http://numpy.org/).

# Appendix A Does the CMU Model Produce Streams?

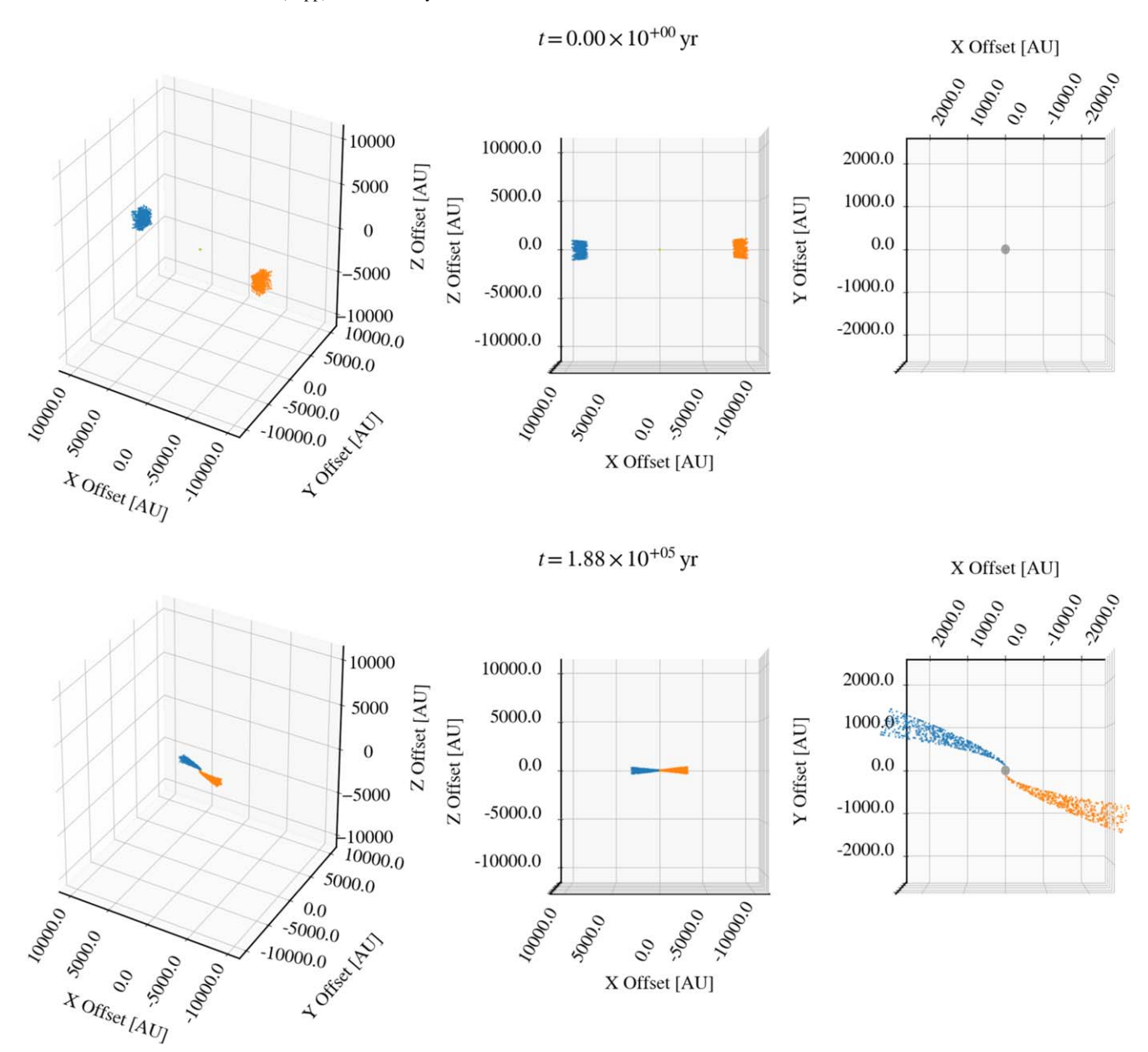
The CMU model produces the trajectory path of a particle over a certain amount of time, while in reality, observational data give us a snapshot in time. Therefore, one important question we need to answer is whether or not the CMU model can produce a stream-like structure from a patch of infalling particles. To do this, we created three "simulations" of varioussized clumps of randomly distributed particles by changing the values of  $r_0$ ,  $\theta_0$ , and  $\phi_0$  (Table A1). The stellar (point) mass  $(M_*)$  and centrifugal radius  $(r_c)$  are kept at a constant for each simulation. We increase the number of particles  $(N_{\text{particles}})$  as we increase the size of the initial clumps. We run each simulation until the final time at which all of the particles are greater than the centrifugal radius,  $r_c$ . All of our simulations produce clear streams when the clumps of particles are about to collide with the disk (see Figures A1, A2 and A3). This is due to the fact that, because the gravitational force at inner radii is greater than at the outer radii, the velocity at the inner radii will increase faster and stretch out the clump as it gets closer to the disk to produce a stream. The streams vary in size based on the initial size of the clump.

 Table A1

 CMU Simulations for Different-sized Clumps of Particles

	r <sub>0</sub> Range (au)	$\theta_0$ Range (°)	$\phi_0$ Range (°)	$M_* \ (M_{\odot})$	r <sub>c</sub> (au)	$N_{ m particles}$	$t_{\text{final}} \times 10^5 \text{ yr}$	Streams?
Simulation 1	8500-9800	85–95	0-10, 180-190	0.1	100	500	1.88	Yes
Simulation 2	7800-9800	70-110	0-25, 180-205	0.1	100	1000	1.65	Yes
Simulation 3	5800-9800	60–120	0-35, 180-215	0.1	100	1500	1.06	Yes

**Notes.** The columns of  $r_0$ ,  $\theta_0$ , and  $\phi_0$  represent the initial radius of the particle, polar angle range of the particles, and azimuthal angle range of the particles. For  $\phi_0$ , the first range corresponds to the orange particles, while the second range corresponds to the blue patch of particles.  $M_*$  and  $r_c$  represent the point mass and centrifugal radius, respectively.  $N_{\text{particles}}$  is the number of particles used in the simulation.  $t_{\text{final}}$  is the final time at which all of the particles radii are greater than the centrifugal radius,  $r_c$ . For each simulation, we label whether or not streams are clearly seen.



**Figure A1.** CMU Model Simulation 1 of infalling particles around a protostar at t=0 yr (top) and the final time at which all of the particles radii are greater than the centrifugal radius,  $r_c$  (bottom). The initial and final times are shown above each figure, respectively. The left panel shows an overall 3D view of the system, the middle panel shows an edge-on view, and the right panel shows a zoomed-in face-on view. The x- and z-axes represent the plane-of-sky axes and the y-axis represents the line-of-sight axis. The gray circles in the rightmost plots indicate the centrifugal radius. An animation of this figure is available. It starts at t=0 yr and ends at at 1.88e +05 yr. The sequence repeats three times, and the real-time duration of the animation is 24 s. (An animation of this figure is available.)

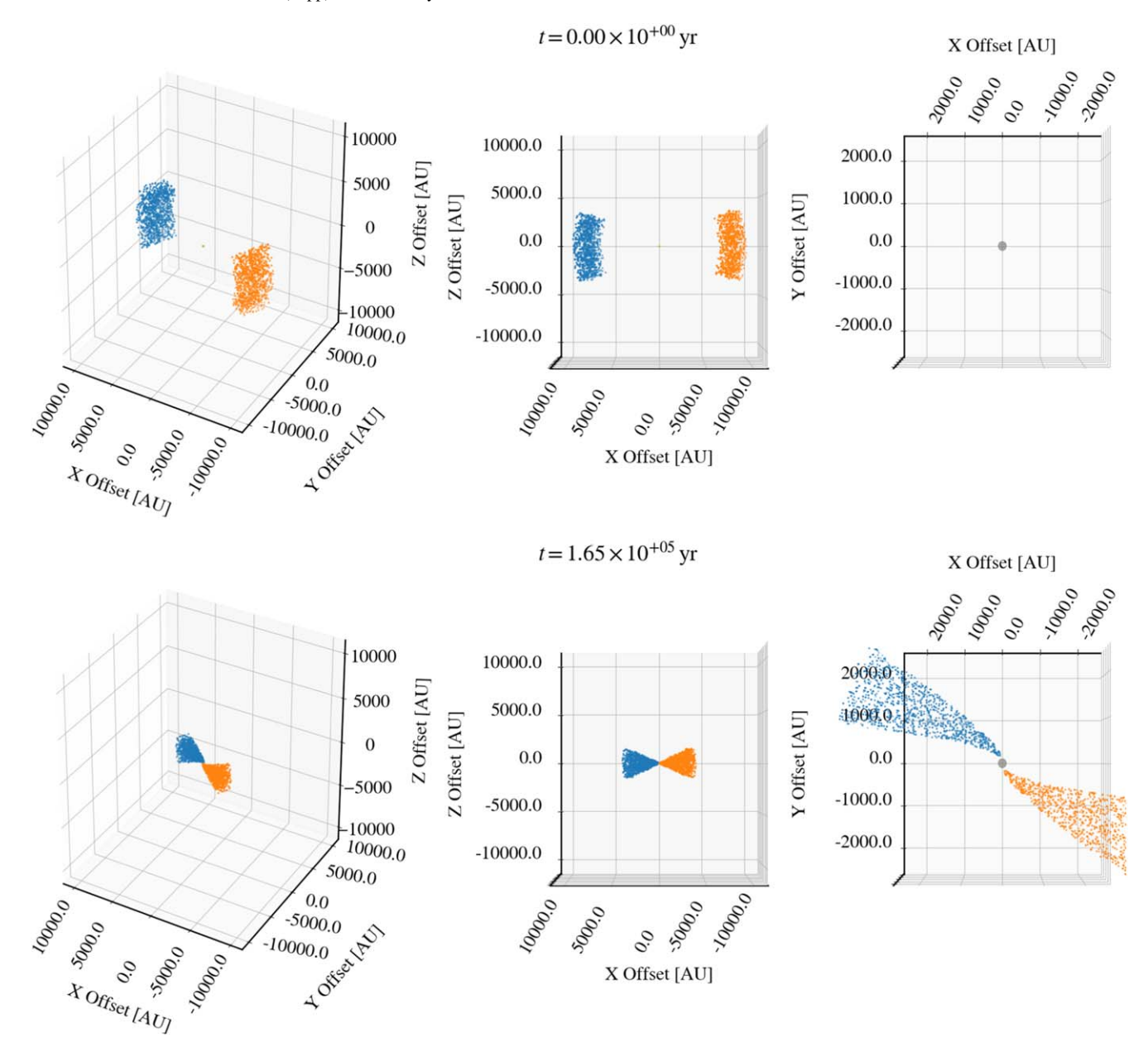


Figure A2. Same as Figure A1, but for Simulation 2. An animation of this figure is available. It starts at t = 0 yr and ends at at 1.65e+05 yr. The sequence repeats three times, and the real-time duration of the animation is 24 s. (An animation of this figure is available.)

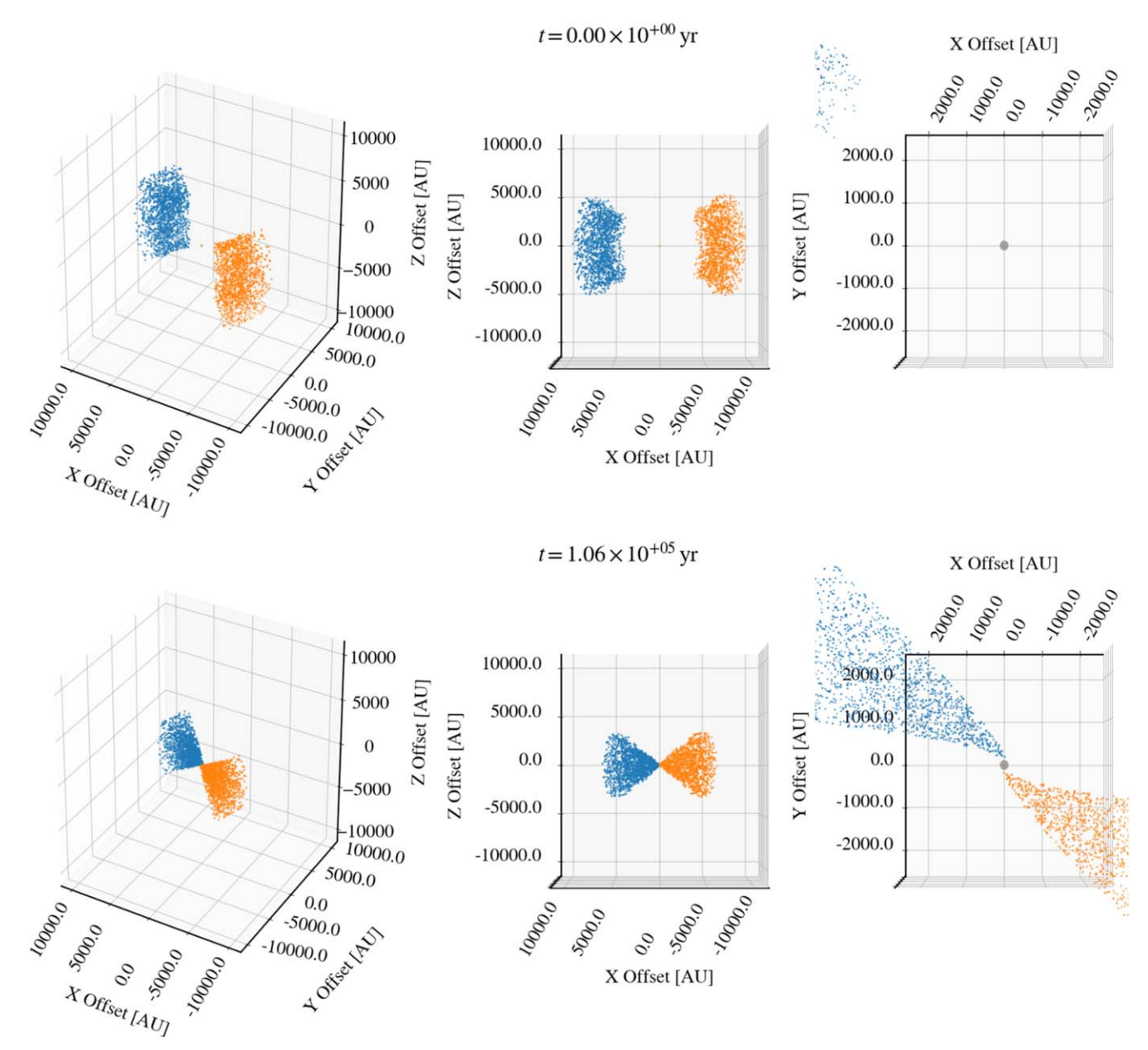


Figure A3. Same as Figure A1, but for Simulation 3. An animation of this figure is available. It starts at t = 0 yr and ends at at 1.06e+05 yr. The sequence repeats three times, and the real-time duration of the animation is 24 s. (An animation of this figure is available.)

#### Appendix B PV Diagrams

To initially assess whether the  $C^{18}O$  emission is connected to the outflow, we make PV cuts parallel and perpendicular to the disk. We produce cuts of 0."5 and 20."0 for each case (Figures B1 and B2). For our cuts along the disk axis (PA = 15°), the velocity structure between the two molecules becomes more noticeable in the larger cut. In the 0."5 cut, the positional extent is similar between  $C^{18}O$  and  $C^{12}CO$ , with the velocity structure overlapping between the two molecules. When we increase the cut to 20."0, we find the  $C^{18}O$  emission to resemble a diamond-like shape, indicative of infalling and rotational motion (see Sakai et al. 2014). On the other hand, the

<sup>12</sup>CO emission in this cut resembles an elongated structure that is more extended along the velocity axis. For our cuts along the outflow axis (PA = 6°), the velocity structure in both cuts shows differences between the molecules. In the 0."5 cut, the C¹8O emission is found in the central part of the PV diagram, while the ¹²CO emission increases in velocity as you move farther away from the center. When we increase the cut to 20."0, we see the same idea that most of the C¹8O emission is centralized, while the ¹²CO emission increases in velocity as you move further away. In this figure, though, some of the C¹8O emission appears to follow the edges of the outflows on the redshifted side. Therefore, we think that this method of disentangling the C¹8O and ¹²CO emission can be more confused and less robust.

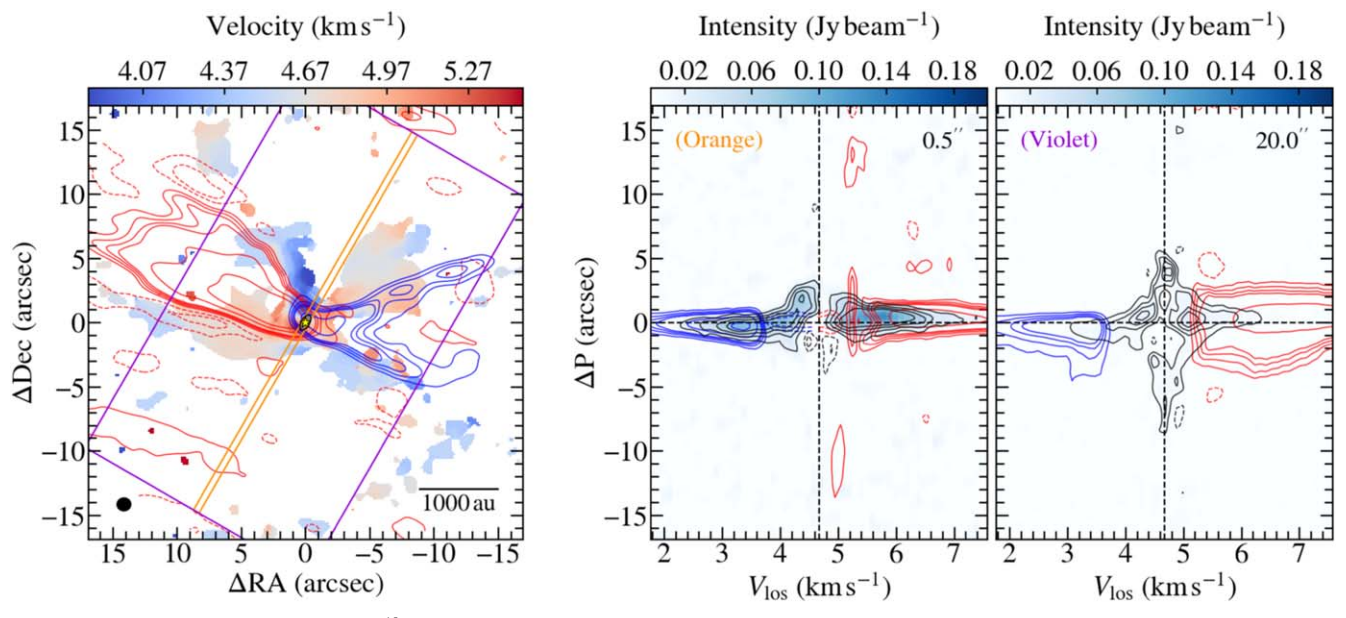
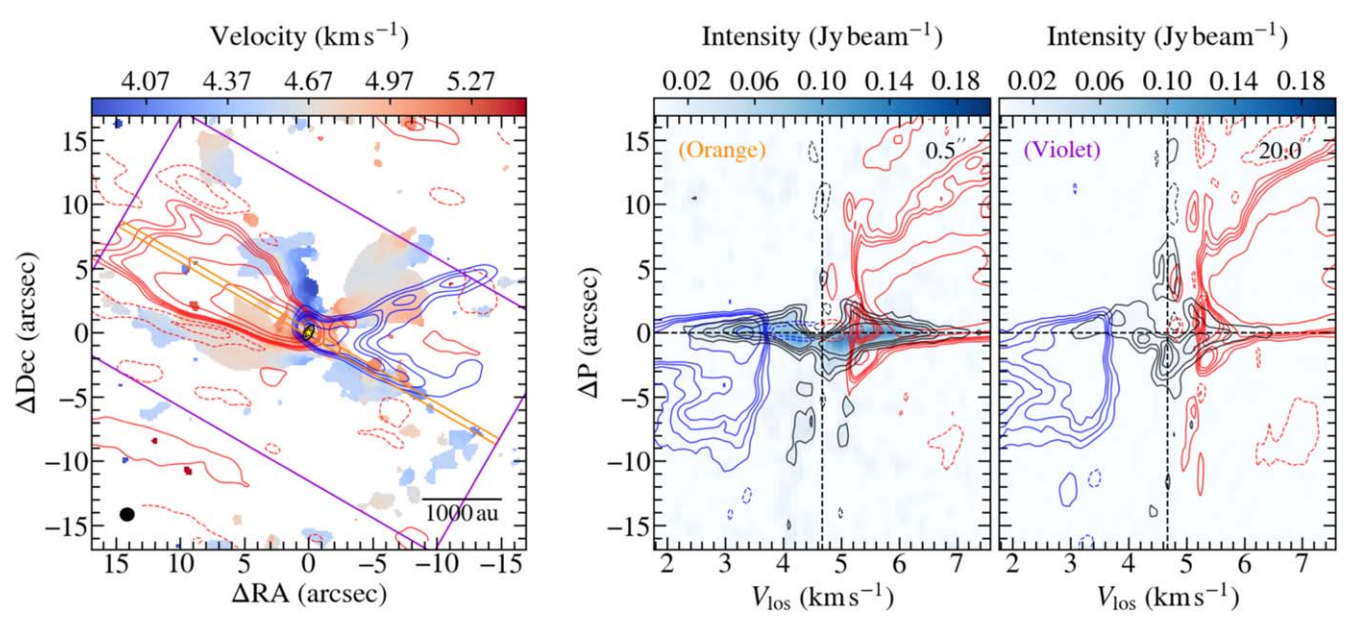


Figure B1. Position–velocity (PV) cuts of our  $C^{18}O$  data along the disk axis. The PA of disk axis is  $15^{\circ}$ . We show the positions and sizes of the PV cuts overlaid on the intensity-weighted velocity map (left). The two widths of the cuts are  $0.7^{\circ}$ 5 (orange) and  $20.7^{\circ}$ 0 (purple), both with lengths of 35v0. We show the  $C^{18}O$  PV diagrams (center and right) for each cut width, with black contours representing levels of  $-10\sigma$ ,  $-5\sigma$ ,  $5\sigma$ ,  $10\sigma$ ,  $15\sigma$ ,  $20\sigma$ ,  $50\sigma$ , and  $100\sigma$ , where  $\sigma = 3.59$  ( $0.7^{\circ}$ 5) and 0.91 ( $20.7^{\circ}$ 0) mJy beam $^{-1}$ . We overplot the  $^{12}CO$  contours in red and blue for the red- and blueshifted outflows, respectively, with the same contour levels as in  $C^{18}O$ , but  $\sigma = 11.04$  ( $0.7^{\circ}$ 5) and 6.20 ( $20.7^{\circ}$ 0) mJy beam $^{-1}$ . All  $\sigma$  values were calculated from a square region in the PV image with no emission.



**Figure B2.** Same as Figure B1, but the cut is taken along the outflow axis. Although the PA of both outflows is given by Yen et al. (2017a), we just take the PA to be the PA of the disk axis minus 9° for simplicity. For the C<sup>18</sup>O contours,  $\sigma = 3.19$  (0... 5) and 0.84 (20... 0) mJy beam -1. For the <sup>12</sup>CO contours,  $\sigma = 9.48$  (0... 5) and 2.33 (20... 0) mJy beam -1.

## Appendix C Column Density Maps

We produce C<sup>18</sup>O column density maps under the local thermal equilibrium (LTE) assumption using the equations and values given in Mangum & Shirley (2015). We first make integrated-intensity maps of our five dendrogram structures. Then, we use the values from those maps and calculate the LTE

column density via

$$N_{\text{tot}} = \frac{3c^2}{16\pi^3 \Omega_s S \mu^2 \nu^3} \left( \frac{Q_{\text{rot}}}{g_J g_K g_I} \right) \exp \left( \frac{E_u}{k T_{\text{ex}}} \right) \int S_{\nu} \Delta \nu,$$

where where  $\Omega_s$  is the beam solid angle assuming a Gaussian-shaped source in sr  $(\Omega_s = 1.133\theta_{\rm maj}\theta_{\rm min})$ , where  $\theta_{\rm maj}$  &  $\theta_{\rm in}$  are

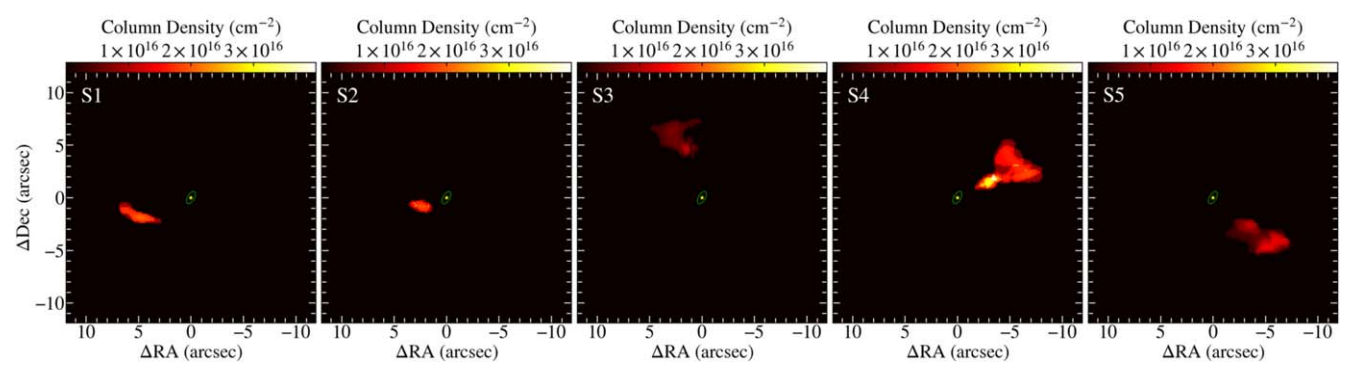


Figure C1. Column density maps for each dendrogram structure. The central source is marked by the yellow star, and the rotationally supported disk is marked by the green circle.

in rad), S is the line strength (for a linear molecular transition from  $J_u \rightarrow J_u - 1$ ,  $S = \frac{J_u^2}{J_u(2J_u + 1)}$ , where  $J_u$  is the upper rotational quantum number),  $\mu$  is the molecular dipole moment in Debye (1 Debye =  $10^{-18}$  statC·cm, and 1 statC = 1 cm<sup>3/2</sup>  $g^{1/2} s^{-1}$ ),  $\nu$  is the rest frequency of the molecule in GHz,  $Q_{rot}$  is the rotational partition function (for diatomic linear molecules, it can be approximated as  $Q_{\rm rot} \simeq \frac{kT}{hB_0} + \frac{1}{3}$ ),  $B_0$  is the rigid rotor rotation constant in MHz,  $g_J$  is the rotational degeneracy due to the projection of the angular momentum on the spatial axis z  $(g_J = 2J_u + 1)$ ,  $g_K$  is the K degeneracy associated with the internal quantum number K in symmetric and asymmetric top molecules due to projections of the total angular momentum onto a molecular axis ( $g_K = 1$  for all linear and asymmetric top molecules),  $g_I$  is the nuclear spin degeneracy that takes account of the statistical weights associated with identical nuclei in a nonlinear molecule with symmetry  $(g_I = \frac{g_{\text{nuclear}}}{g_n})$  and  $g_I = 1$  for linear molecules),  $E_u$  is the upper energy level in Kelvin,  $T_{\text{ex}}$  is the excitation temperature in Kelvin,  $S_{\nu}$  is the flux density in Jy, and  $\Delta v$  is the velocity resolution in km s<sup>-1</sup>. We assume  $T_{\rm ex}$  to be 30 K, the temperature of the dust continuum emission recently derived by Vazzano et al. (2021). For C<sup>18</sup>O, we use

$$B_0 = 57,635.96 \text{ MHz}$$
 $T_{\text{ex}} = 30 \text{ K}$ 
 $\mu = 0.11079 \text{ Debye}$ 
 $J_u = 2$ 
 $g_J = 2J_u + 1$ 
 $g_K = 1$ 
 $g_I = 1$ 
 $E_u = 15.08 \text{ K}$ 
 $S = \frac{J_u}{2J_u + 1}$ 
 $\nu = 219.56036 \text{ GHz}$ 

to plug into the column density equation and make the maps shown in Figure C1.

#### ORCID iDs

Travis J. Thieme https://orcid.org/0000-0003-0334-1583 Shih-Ping Lai https://orcid.org/0000-0001-5522-486X Sheng-Jun Lin https://orcid.org/0000-0002-6868-4483

Chin-Fei Lee https://orcid.org/0000-0002-3024-5864 Hsi-Wei Yen https://orcid.org/0000-0003-1412-893X Zhi-Yun Li https://orcid.org/0000-0002-7402-6487 Ka Ho Lam https://orcid.org/0000-0003-3581-1834 Bo Zhao https://orcid.org/0000-0002-5359-8072

#### References

```
Aso, Y., Ohashi, N., Aikawa, Y., et al. 2017, ApJ, 849, 56
Astropy Collaboration, Price-Whelan, A. M., Sipőcz, B. M., et al. 2018, AJ,
  156, 123
Astropy Collaboration, Robitaille, T. P., Tollerud, E. J., et al. 2013, A&A,
  558, A33
Bergin, E. A., & Tafalla, M. 2007, ARA&A, 45, 339
Cassen, P., & Moosman, A. 1981, Icar, 48, 353
Cheong, P.-I. 2018, Master's thesis, National Tsing Hua Univ., Taiwan
Chevalier, R. A. 1983, ApJ, 268, 753
Codella, C., Cabrit, S., Gueth, F., et al. 2014, A&A, 568, L5
Dunham, M. M., Arce, H. G., Allen, L. E., et al. 2013, AJ, 145, 94
Dzib, S. A., Loinard, L., Ortiz-León, G. N., Rodríguez, L. F., & Galli, P. A. B.
  2018, ApJ, 867, 151
Evans, Neal J., I., Dunham, M. M., Jørgensen, J. K., et al. 2009, ApJS,
   181, 321
Frerking, M. A., Langer, W. D., & Wilson, R. W. 1982, ApJ, 262, 590
Gaudel, M., Maury, A. J., Belloche, A., et al. 2020, A&A, 637, A92
Harsono, D., Jørgensen, J. K., van Dishoeck, E. F., et al. 2014, A&A, 562, A77
Hennebelle, P., & Ciardi, A. 2009, A&A, 506, L29
Hennebelle, P., & Fromang, S. 2008, A&A, 477, 9
Hsieh, C.-H., Lai, S.-P., Cheong, P.-I., et al. 2020, ApJ, 894, 23
Hull, C. L. H., Le Gouellec, V. J. M., Girart, J. M., Tobin, J. J., & Bourke, T. L.
  2020, ApJ, 892, 152
Hunter, J. D. 2007, CSE, 9, 90
Joos, M., Hennebelle, P., Ciardi, A., & Fromang, S. 2013, A&A, 554, A17
Kuffmeier, M., Zhao, B., & Caselli, P. 2020, A&A, 639, A86
Lam, K. H., Li, Z.-Y., Chen, C.-Y., Tomida, K., & Zhao, B. 2019, MNRAS,
   489, 5326
Le Gouellec, V. J. M., Hull, C. L. H., Maury, A. J., et al. 2019, ApJ, 885, 106
Lee, C.-F., Hirano, N., Zhang, Q., et al. 2014, ApJ, 786, 114
Lee, C.-F., Mundy, L. G., Reipurth, B., Ostriker, E. C., & Stone, J. M. 2000,
Lee, Y.-N., Charnoz, S., & Hennebelle, P. 2021, A&A, 648, A101
Li, Z.-Y., Krasnopolsky, R., & Shang, H. 2011, ApJ, 738, 180
Li, Z.-Y., Krasnopolsky, R., & Shang, H. 2013, ApJ, 774, 82
Li, Z.-Y., Krasnopolsky, R., Shang, H., & Zhao, B. 2014, ApJ, 793, 130
Lommen, D., Jørgensen, J. K., van Dishoeck, E. F., & Crapsi, A. 2008, A&A,
  481, 141
Machida, M. N., Matsumoto, T., & Inutsuka, S.-i. 2016, MNRAS, 463, 4246
Mangum, J. G., & Shirley, Y. L. 2015, PASP, 127, 266
McMullin, J. P., Waters, B., Schiebel, D., Young, W., & Golap, K. 2007, in
   ASP Conf. Ser. 376, Astronomical Data Analysis Software and Systems
  XVI, ed. R. A. Shaw, F. Hill, & D. J. Bell (San Francisco, CA: ASP), 127
Mellon, R. R., & Li, Z.-Y. 2008, ApJ, 681, 1356
Motte, F., & André, P. 2001, A&A, 365, 440
Murillo, N. M., Harsono, D., McClure, M., Lai, S. P., & Hogerheijde, M. R.
```

2018, A&A, 615, L14

```
Murillo, N. M., Lai, S.-P., Bruderer, S., Harsono, D., & van Dishoeck, E. F.
  2013, A&A, 560, A103
Murillo, N. M., van Dishoeck, E. F., Hacar, A., Harsono, D., & Jørgensen, J. K.
  2021, arXiv:2111.04039
Ohashi, N., Saigo, K., Aso, Y., et al. 2014, ApJ, 796, 131
Pineda, J. E., Segura-Cox, D., Caselli, P., et al. 2020, NatAs, 4, 1158
Pineda, J. E., Zhao, B., Schmiedeke, A., et al. 2019, ApJ, 882, 103
Robitaille, T., Rice, T., Beaumont, C., et al. 2019, astrodendro: Astronomical
   data dendrogram creator, Astrophysics Source Code Library, ascl:1907.016
Rosolowsky, E. W., Pineda, J. E., Kauffmann, J., & Goodman, A. A. 2008,
    ApJ, 679, 1338
Sakai, N., Sakai, T., Hirota, T., et al. 2014, Natur, 507, 78
Sakai, N., & Yamamoto, S. 2013, ChRv, 113, 8981
Seifried, D., Banerjee, R., Pudritz, R. E., & Klessen, R. S. 2013, MNRAS,
  432, 3320
Seifried, D., Banerjee, R., Pudritz, R. E., & Klessen, R. S. 2015, MNRAS,
```

```
Shu, F. H. 1977, ApJ, 214, 488
Tachihara, K., Rengel, M., Nakajima, Y., et al. 2007, ApJ, 659, 1382
```

446, 2776

```
Terebey, S., Shu, F. H., & Cassen, P. 1984, ApJ, 286, 529
Tobin, J. J., Hartmann, L., Bergin, E., et al. 2012a, ApJ, 748, 16
Tobin, J. J., Hartmann, L., Chiang, H.-F., et al. 2012b, Natur, 492, 83
Tsukamoto, Y., Okuzumi, S., Iwasaki, K., Machida, M. N., & Inutsuka, S.
  2018, ApJ, 868, 22
Ulrich, R. K. 1976, ApJ, 210, 377
van der Walt, S., Colbert, S. C., & Varoquaux, G. 2011, CSE, 13, 22
Vazzano, M. M., Fernández-López, M., Plunkett, A., et al. 2021, A&A,
  648, A41
Williams, J. P., & Cieza, L. A. 2011, ARA&A, 49, 67
Wurster, J., Bate, M. R., & Price, D. J. 2018, MNRAS, 476, 2063
Wurster, J., & Lewis, B. T. 2020, MNRAS, 495, 3795
Wurster, J., Price, D. J., & Bate, M. R. 2016, MNRAS, 457, 1037
Yen, H.-W., Gu, P.-G., Hirano, N., et al. 2019, ApJ, 880, 69
Yen, H.-W., Koch, P. M., Takakuwa, S., et al. 2015, ApJ, 799, 193
Yen, H.-W., Koch, P. M., Takakuwa, S., et al. 2017a, ApJ, 834, 178
Yen, H.-W., Takakuwa, S., Chu, Y.-H., et al. 2017b, A&A, 608, A134
Yen, H.-W., Takakuwa, S., Ohashi, N., et al. 2014, ApJ, 793, 1
Zhao, B., Caselli, P., Li, Z.-Y., et al. 2016, MNRAS, 460, 2050
```